Tracing Extreme Updrafts in Hurricane Wilma (2005) to Their Boundary Layer Roots Using Trajectories: A Thermodynamic and Structural Analysis

WILLIAM MILLER[a] AND DA-LIN ZHANG

Department of Atmospheric and Oceanic Science, University of Maryland, College Park, College Park, Maryland

(Manuscript received 23 September 2019, in final form 30 April 2020)

ABSTRACT

This study uses a recently developed trajectory model to trace eyewall updrafts in a high-resolution Hurricane Wilma (2005) prediction to their roots in the maritime boundary layer (MBL) in order to better understand their thermodynamics and how they interact with the swirling winds. Out of 97 020 four-hour backward trajectories seeded from the upper troposphere, the 45% of them originating from the MBL are stratified into five subsamples binned by peak vertical velocity w_{MAX}. Of particular interest are the thermodynamic characteristics of parcels belonging to the w_{MAX}-Extreme subsample (i.e., those with w_{MAX} exceeding 20 m s^{-1}) that ascend through Wilma's strongest convective burst (CB) cores. A vertical momentum budget computed along a selected w_{MAX}-Extreme trajectory confirms that the parcel possesses large positive buoyancy that more than compensates for negative hydrometeor loading to yield an upper-tropospheric $w_{MAX} \sim 30$ m s^{-1}. Comparing all 1170 w_{MAX}-Extreme trajectories with all 19 296 secondary circulation trajectories shows that the former tends to originate from the MBL where equivalent potential temperature θ_e and ocean surface heat and moisture fluxes are locally enhanced. The w_{MAX}-Extreme parcels become further differentiated from the background ascent in terms of their (i) greater updraft width and smaller θ_e reduction while ascending into the midtroposphere, implying lower environmental entrainment rates, and (ii) less hydrometeor loading in the $z = 3$–5-km layer. The Lagrangian analysis herein bridges two previous studies that focused separately on the importance of high SSTs and fusion latent heat release to the development of CBs, the latter of which may facilitate upper-level warm core development through their compensating subsidence.

1. Introduction

Observations of tropical cyclones (TCs) over recent decades have shown that outbreaks of inner-core deep convection, the so-called convective bursts (CBs), often precede or coincide with episodes of rapid intensification (RI), defined for Atlantic TCs as a maximum surface wind speed V_{MAX} intensification rate exceeding 15 m s^{-1} (24 h)$^{-1}$ (Kaplan and DeMaria 2003). Gentry et al. (1970) identified these features as localized cold brightness temperature anomalies in satellite imagery and recognized their potential significance in the TC intensification process. Subsequent studies used airborne Doppler radar and flight-level temperature instrumentation to analyze CB three-dimensional kinematic structure and thermodynamics (Rodgers et al. 1998; Heymsfield et al. 2001; Molinari et al. 2006; Houze et al. 2009; Guimond et al. 2010, 2016). Convection-resolving numerical TC simulations have captured similar features (Chen and Zhang 2013; Chen and Gopalakrishnan 2015; Nguyen and Molinari 2015; Hazelton et al. 2017).

Previous studies have proposed several mechanisms through which inner-core CBs may facilitate TC intensification. According to one hypothesis, compensating subsidence flanking the inner edges of CB updrafts enhances development of the warm core. Heymsfield et al. (2001) showed how a cluster of CB subsidence currents originating near the tropopause may have contributed up to 3°C of midlevel eye warming in Hurricane Bonnie (1998). Provided that adiabatic warming offsets evaporative cooling in subsidence currents, the high inertial stability inside of the radius of maximum wind (RMW) may help trap subsidence-induced warm air in the eye (Hack and Schubert 1986). CBs or "hot towers" may also facilitate tropical cyclogenesis by moistening the inner-core midtroposphere, thereby "priming" it for the

[a] Current affiliation: Cooperative Institute for Mesoscale Meteorological Studies, University of Oklahoma, National Severe Storms Lab, Norman, Oklahoma.

Corresponding author: Dr. William Miller, wmiller1@umd.edu

DOI: 10.1175/MWR-D-19-0303.1

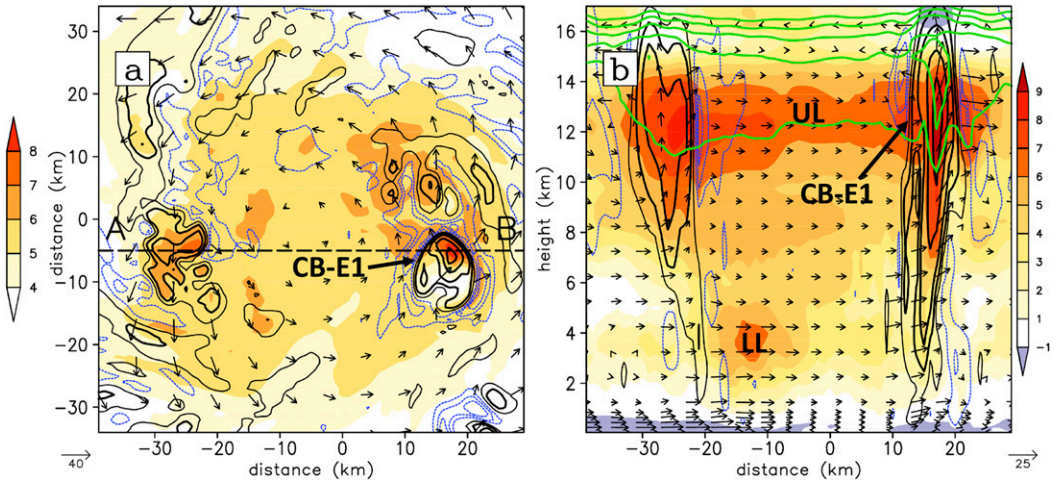

FIG. 1. (a) WRF-predicted temperature anomaly $T'(z, t)$ (shaded; K) at forecast time t = 16:10 and z = 14 km, computed with respect to the 1000 km × 1000 km area-averaged temperature profile centered on the storm at the initial time $\overline{T}(z, t = 0)$. Vertical velocity is contoured (thin black at 2 m s^{-1}; thick black at 5, 10, 20, and 30 m s^{-1}; dotted blue at −5, −3, and −1 m s^{-1}) and horizontal storm-relative flow vectors (m s^{-1}) are also shown. (b) Vertical cross section, taken along the dashed line A–B, given in (a), of $T'(z, t)$ (shaded) as defined in (a), θ (contoured in green every 5 K over the range 360–380 K), and vertical velocity contoured as in (a), with in-plane storm-relative flow vectors (m s^{-1}). Symbols LL and UL highlight the locations of the lower-level and upper-level warm cores, respectively, and symbol CB-E1 labels the CB updraft element discussed in the text. Note the different shading scales used for $T'(z, t)$ in (a) and (b).

subsequent development of sustained convection (Nolan 2007; Montgomery et al. 2006). Other studies have shown how CBs embedded in a developing TC circulation can spin up the tangential wind v_t by collectively aggregating and stretching low-level cyclonic vorticity anomalies (Nguyen et al. 2008; Montgomery and Smith 2014; Nguyen and Molinari 2015).

Hurricane Wilma (2005) underwent a record-breaking 12-h RI event on 18–19 October, featuring a V_{MAX} intensification rate of 39 m s^{-1} (12 h)$^{-1}$ that led to a peak V_{MAX} of 82 m s^{-1}. Wilma intensified in the western Caribbean under near-ideal environmental conditions with low vertical wind shear (VWS) and high sea surface temperatures (SSTs) of 29°–30°C. The storm subsequently underwent an eyewall replacement cycle and weakened to Saffir–Simpson category 4 intensity before making landfall on Cozumel Island near Mexico's Yucatan Peninsula on 21 October; see Pasch et al. (2006) for more details.

Chen et al. (2011, hereafter CZ11) generated a cloud-permitting prediction of Hurricane Wilma (2005) using the Weather Research and Forecasting (WRF) Model (Skamarock et al. 2008). Using this dataset, Zhang and Chen (2012) demonstrated how upper-tropospheric eye warming accounted for the largest portion of Wilma's hydrostatically induced minimum central sea level pressure P_{MIN} falls during RI. Chen and Zhang (2013, hereafter CZ13) showed how CBs, which they defined as updraft grid columns with $w \geq 15$ m s^{-1} above z = 11 km, directed subsidence into the developing upper-level warm core around RI onset; Fig. 1 shows an example of this process. Miller et al. (2015, hereafter M15) found that turning off the latent heat of fusion resulted in a storm with fewer CBs and reduced upper-level warming that produced a less extreme RI rate. They also used a heat budget to show that Wilma's upper-level eye warming occurred primarily under adiabatic conditions.

On the vortex scale, eyewall vertical ascent connects the low-level radial inflow to the upper-level outflow, thus comprising the middle branch of the TC "secondary circulation." Early theories of TC intensification (Charney and Eliassen 1964; Ooyama 1969, 1982; Shapiro and Willoughby 1982; Hack and Schubert 1986) recognized the significance of the secondary circulation in converting latent heat energy released by inner-core deep convection into the swirling winds' kinetic energy; however, they generally assumed eyewall ascent to be relatively weak, horizontally uniform, and constrained by balanced vortex dynamics. Over recent decades, however, observations and high-resolution modeling of TC eyewalls have found considerable horizontal variation in the vertical velocity w fields, even for mature cases (Jorgensen 1984; Jorgensen et al. 1985; Marks and Houze 1987; Black et al. 1996; Braun 2002; Eastin et al. 2005a,b; Braun et al. 2006; Hogsett and Zhang 2009; Rogers 2010; Rogers et al. 2015). All of these studies reported localized "cores" of stronger updrafts

as well as downdrafts being embedded within a weaker background ascent. Furthermore, Braun (2002) and Eastin et al. (2005a,b) showed that the updraft cores could be positively buoyant relative to the mesoscale eyewall environment, which implies the existence of conditional instability in the eyewall. M15 found that azimuthally averaged slantwise convective available potential energy (SCAPE) computed along constant absolute angular momentum {AAM = $r[(v_t + fr)/2]$, where r and f are the radius and Coriolis parameter, respectively} surfaces exceeded 400 J kg^{-1} in their simulated Hurricane Wilma (2005) eyewall during RI. Assuming pseudoadiabatic thermodynamics and undilute ascent, SCAPE of this magnitude would support a theoretical maximum updraft speed $w_{\text{MAX-UNDILUTE}} \cong \sqrt{2\text{SCAPE}} = 28\,\text{m s}^{-1}$, which is comparable to the strongest CB updrafts found in their prediction. In contrast, the wind-induced surface heat exchange (WISHE) theory of TC intensification (Rotunno and Emanuel 1987; Emanuel 1997) is based upon the steady-state Emanuel (1986) model which assumes that any developing pockets of eyewall SCAPE become immediately consumed, thus rendering the axisymmetric eyewall neutral to moist pseudoadiabatic ascent. Perhaps most significantly, WISHE theory refocused attention on heat and moisture fluxes from the ocean surface as the primary source of high equivalent potential temperature θ_e air in a TC maritime boundary layer (MBL). Further work is needed toward developing a more complete TC intensification model that incorporates the impacts of buoyant deep convection and unbalanced dynamics with insights gained from older theories that assumed balanced dynamics (Charney and Eliassen 1964; Ooyama 1982; Emanuel 1986) and moist neutral thermodynamics (Emanuel 1986).

The major objective of this study is to better understand the thermodynamics and three-dimensional structure of intense updrafts found in the cores of Hurricane Wilma's (2005) CBs. It is still unclear how a TC eyewall can support large parcel buoyancy. While wind-induced heat and moisture fluxes above warm SSTs provide an ample source of high θ_e air to a TC MBL (Emanuel 1986; Braun 2002; Zhang et al. 2002; Cram et al. 2007), excessive hydrometeor loading in a moist tropical environment (Zhang et al. 2000) and prior vortex-scale warming from latent heat release (LHR) (Emanuel 1986) could both render the eyewall a less favorable environment for maintaining buoyant updrafts. Cram et al. (2007) showed how ventilation of the sheared Hurricane Bonnie (1998) eyewall reduced axisymmetric midlevel eyewall θ_e by ~1 K; midtropospheric minima in azimuthally averaged θ_e have also been found in other simulated mature TC eyewalls (Liu et al. 1999; Braun 2002). Ventilation-induced cooling of the midlevel environment could enhance eyewall updraft buoyancy, provided entrainment[1] of surrounding eyewall air into updrafts remains limited. For context, consider Zipser (2003)'s finding that the observed tendency for tropical oceanic convective updrafts outside of TC eyewalls to be considerably weaker than continental severe storm updrafts could not be fully explained by differences in their respective environmental soundings. Rather, he argued that oceanic updrafts' greater departures from the theoretical undilute w_{MAX} results from greater environmental air entrainment into their narrower cores. Therefore, we ask: how significant a role does entrainment play in regulating Hurricane Wilma's (2005) eyewall updraft intensity? A few other questions are worth addressing. Given the rapidly rotating flows, to what extent can CB core updraft roots be traced to portions of the MBL where ocean surface heat fluxes are locally higher? How do CB core updrafts interact with the locally sheared (both horizontally and vertically) swirling winds? Do local pressure perturbations from hydrostatic balance significantly impact parcel accelerations in CB cores?

Unlike in many previous studies,[2] the abovementioned objective will be achieved in a Lagrangian framework by using the Miller and Zhang (2019, hereafter MZ19) trajectory model to run a large batch of backward trajectories from the CZ11 Wilma (2005) WRF prediction that samples both CB updraft cores and the background secondary circulation. Herein we shall use the hh:mm format when describing forecast times measured from the model initialization. We focus on the 12:00–20:00 prediction period, which features intense inner-core CB activity, RI onset at 15:00, and the subsequent RI in V_{MAX} from 38 to 58 m s^{-1}. Wilma undergoes significant structural changes over this period (e.g., the axisymmetrization and contraction of the eyewall convection) (see Figs. 12a–c in CZ11) and the intensification of the upper-level warm core (see Fig. 1a in CZ13). Our study combines (i) a detailed structural and thermodynamic comparison of a CB core updraft with another updraft more representative of the background secondary circulation, with (ii) a statistical comparison of thermodynamic variables averaged over subsamples of trajectories binned by updraft intensity. The latter approach provides robust statistics and it should mitigate, to some extent, random trajectory position errors

[1] Hereafter, we use the term "entrainment" when referring to air exchange between updrafts and their surrounding eyewall environment, as opposed to "ventilation," which refers to air exchange on the vortex scale between the eyewall and its surroundings.

[2] A few previous studies have used trajectories to investigate TC eyewall updraft thermodynamics, which include Braun (2002), Cram et al. (2007), and Hazelton et al. (2017).

stemming from temporal interpolation of the 5-min WRF output winds to the 10-s trajectory computational time step.

The next section describes the Hurricane Wilma (2005) WRF prediction, trajectory computation methods, experiment design, and statistical methods used for analyzing trajectory output variables. Section 3 compares the two representative CB core and background secondary circulation trajectories in detail, and section 4 uses a large trajectory sample to show how thermodynamic properties, environmental air entrainment, and vertical accelerations vary with updraft intensity. A summary and concluding remarks are given in the final section.

2. Data and methodology

a. Hurricane Wilma (2005) WRF prediction

CZ11 describe their Wilma (2005) WRF prediction configuration and observation validations in detail. They integrated the WRF Advanced Research core (ARW) for 72 h beginning at 0000 UTC 18 October 2005, using a two-way interactive, quadruply nested (27, 9, 3, and 1 km) grid, 55 vertical σ levels, and a 30-hPa model top. This prediction captures the timing, location and rate of Wilma's observed RI and subsequent eyewall replacement cycle reasonably well, along with the associated inner-core structural changes.

b. Trajectory computations

Trajectories are computed from the Wilma WRF prediction 5-min output flow fields using the algorithm developed by MZ19. First, WRF 1-km domain 12:00–20:00 output is transferred to an unstaggered grid and vertically interpolated to height coordinates using ARWpost software.[3] The resulting "computational grid" has a vertical resolution of 250 m (50 m) above (below) $z = 1$ km, with a top boundary of $z = 20$ km and a bottom level populated with WRF-output 10-m horizontal winds and zero w. The MZ19 model integrates parcel positions using a second order Runge–Kutta (RK2) scheme with a 10-s computational time step. Gridded winds are interpolated to the parcel positions trilinearly in space; time interpolations from the two nearest WRF output times use advection correction (AC; Gal-Chen 1982; Shapiro et al. 2015; MZ19), a technique that interpolates data in a reference frame that follows the mean flow, rather than from a fixed position as in traditional linear time interpolation (LI). More specifically, time interpolations use the AC_W algorithm described in MZ19, where AC is used for scalars and w, while LI is used for the u and v components. Choice of AC_W is motivated by the fact that between 5-min output times over the analysis period, Wilma's inner-core horizontal winds remain relatively steady whereas deep convective updrafts translate considerable azimuthal distances (to be shown in section 3). Any backward trajectories arriving at the computational grid top or lateral boundaries are flagged and their integration is terminated early. Scalar variables interpolated to the 10-s trajectory positions (Table 1) are saved for analysis.

TABLE 1. Diagnostic variables interpolated from the postprocessed WRF grid to trajectory positions during trajectory computations.

Symbol	Description	Units
w	Vertical velocity	m s^{-1}
T	Temperature	K
p	Pressure	hPa
θ_e	Equivalent potential temperature (Bolton 1980)	K
q_V	Water vapor mixing ratio	g kg^{-1}
q_{LIQ}	Combined liquid hydrometeor (cloud + rainwater) mixing ratio	g kg^{-1}
q_{FRZ}	Combined frozen hydrometeor (ice + snow + graupel) mixing ratio	g kg^{-1}

c. Trajectory experiment design and statistical analysis techniques

For each WRF output time between 16:00 and 20:00, a set of 1980 4-h backward trajectories is seeded from $z = 14$ km over the region where the eyewall updraft core flares outward, forming the roots of the main outflow. Seed points are positioned at 2° azimuthal intervals on concentric rings radially spaced every 2 km over a 20-km-wide annulus centered on the $z = 14$ km RMW (Fig. 2a). Of all 97 020 backward trajectories, only the ~45% that can be traced to the MBL—hereafter the MBL-Origin sample—are further analyzed. Herein the MBL is defined as the region below $z = 0.5$ km, which generally aligns with the azimuthally averaged low-level inflow inside of $r = 40$ km over the analysis period (not shown). The remaining trajectories generally originate from either (i) the midlevel eye, eyewall, or outer environment; or (ii) the outflow layer or higher levels. The MBL-Origin trajectories are further stratified into subsamples binned by w_{MAX}, defined for each trajectory as its maximum w over all 10-s output times. These subsamples are named w_{MAX}-8, w_{MAX}-12, w_{MAX}-16, w_{MAX}-20, and w_{MAX}-Extreme, for $w_{MAX} \leq 8$ m s^{-1}, 8 m s^{-1} $< w_{MAX} \leq$ 12 m s^{-1}, 12 m s^{-1} $< w_{MAX} \leq$ 16 m s^{-1}, 16 m s^{-1} $< w_{MAX} \leq$ 20 m s^{-1}, and $w_{MAX} >$ 20 m s^{-1}, respectively. Each MBL-Origin trajectory is assigned an "updraft period" running backward in time, beginning with the

[3] Documentation for the ARWpost software package is available at http://www2.mmm.ucar.edu/wrf/users/docs/user_guide_V3.9/users_guide_chap9.htm#_ARWpost_3 (accessed 5 February 2020).

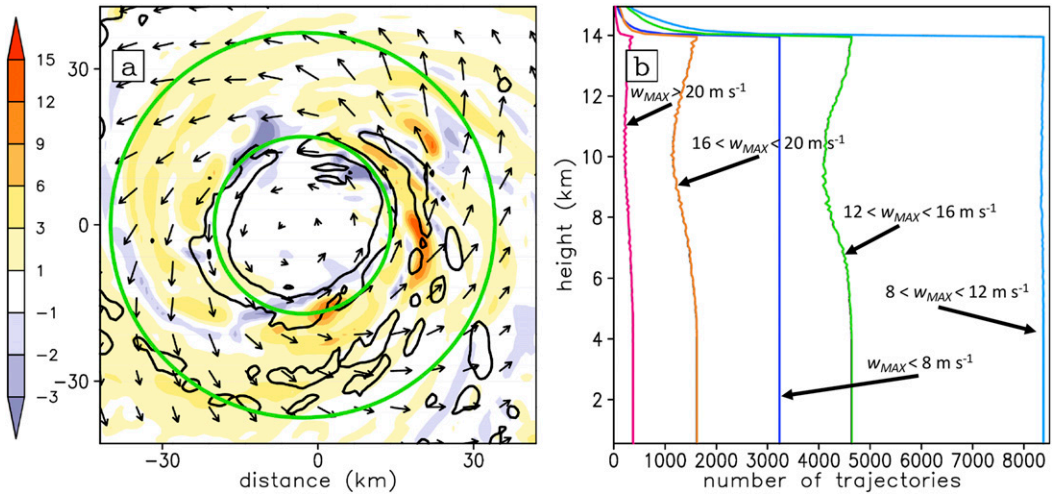

FIG. 2. (a) WRF-predicted z = 14-km vertical velocity w (shaded; m s^{-1}) and horizontal wind vectors (m s^{-1}) with z = 6-km w (2 m s^{-1} contoured in black) at 18:00. Green circles bound the annular region from which backward trajectories are seeded, as described in the text. (b) Number of trajectories in subsamples of w_{MAX}-8, w_{MAX}-12, w_{MAX}-16, w_{MAX}-20, and w_{MAX}-Extreme with at least one output data point contained within the 100-m vertical layer bin configuration used for the vertical momentum budget analysis in section 4d, as shown on the y axis.

first output time for which w averaged over the next 1-min interval exceeds zero (possibly the seed point) and ending with the parcel reaching z = 0.5 km.

Tables 2 and 3 list additional diagnostic variables along trajectories that are computed "offline" (i.e., after completion of trajectory integrations). Whereas Table 2 variables are derived from the trajectory output data, Table 3 variable computations require remapping trajectory positions to the WRF grid in order to obtain data from the parcel's surrounding environment or to interpolate additional WRF fields to the parcel position. Perturbations from the azimuthal mean are denoted with the prime superscript and "360" subscript; primed variables missing the "360" subscript are perturbations from the hydrostatic base state (section 2d). For example, $\theta'_{v,360} = \theta_v - \overline{\theta_{v,360}}$, where $\overline{\theta_{v,360}}$ is the azimuthally averaged virtual potential temperature, interpolated linearly in time and bilinearly in space to the parcel (r, z) coordinates. For any diagnostic variable a, individual trajectory profiles $a(k)$ are generated by averaging a over trajectory output times that fall within each 250-m-height bin $k = 1, k_{TOP}$ spanning the z = 0.25–14-km layer. Mean profiles of a for a given w_{MAX}-binned subsample S may then be computed as

$$\overline{a}^S(k) = \frac{\sum_{i=1}^{n} a_i(k)}{n}, \tag{1}$$

where trajectories $i = 1, \ldots, n$ belong to S and contain at least one output data point within bin k, and $a_i(k)$ is the ith trajectory profile of a. Subsample variance and standard deviation profiles of a are, respectively, given by

$$\hat{a}^S(k) = \frac{\sum_{i=1}^{n} \left[a_i(k) - \overline{a}^S(k)\right]^2}{n-1}, \tag{2}$$

and

$$s_a^S(k) = \left[\hat{a}^S(k)\right]^{1/2}. \tag{3}$$

Differences in $\overline{a}^S(k)$ between different subsamples are evaluated for statistical significance at the two-sided 95% confidence interval using the Student's t test for independent samples (Wilks 2011, 142–144). The subsample Pearson correlation coefficient $\rho_{a,b}^S$ between variables a and b is computed as

$$\rho_{a,b}^S(k) = \frac{\sum_{i=1}^{n} \left[a_i(k) - \overline{a}^S(k)\right]\left[b_i(k) - \overline{b}^S(k)\right]}{(n-1)s_a^S(k)s_b^S(k)}. \tag{4}$$

TABLE 2. Diagnostic variables computed at trajectory positions after completion of trajectory integrations using the Table 1 variables.

Symbol	Description	Units
ρ	Density	kg m^{-3}
θ_v	Virtual potential temperature	K
q_{HYD}	Total hydrometeor mixing ratio ($q_{LIQ} + q_{FRZ}$)	g kg^{-1}
RH	Relative humidity (with respect to ice for $T < 273.15$ K)	%
Dw/Dt	Vertical acceleration	m s^{-2}

TABLE 3. Diagnostic variables computed at trajectory positions after completion of trajectory integrations. Calculation of all variables listed here necessitated remapping trajectory positions to the WRF grid output in either Cartesian or cylindrical coordinates. Asterisks indicate that the variable was bilinearly interpolated to the trajectory horizontal coordinates.

Symbol	Description	Units
w'_{360}	w perturbation from the azimuthal mean	m s^{-1}
$\theta'_{v,360}$	θ_v perturbation from the azimuthal mean	K
$q'_{\mathrm{LIQ},360}$	q_{LIQ} perturbation from the azimuthal mean	g kg^{-1}
$q'_{\mathrm{FRZ},360}$	q_{FRZ} perturbation from the azimuthal mean	g kg^{-1}
PGA	Perturbation vertical pressure gradient acceleration	m s^{-2}
$g\theta'_v/\overline{\theta_v}$	Thermal buoyancy	m s^{-2}
$g(\kappa-1)p'/\overline{p}$	Horizontal perturbation pressure contribution to buoyant acceleration	m s^{-2}
gq'_{HYD}	Hydrometeor loading	m s^{-2}
d_{EDGE}	Smallest distance to updraft edge among the four Cardinal directions	km
D_{AVG}	Mean updraft diameter	km
$\theta_{e,\mathrm{ENV}}$	Environmental θ_e (see section 2e)	K
H_S	Sensible surface heat flux*	W m^{-2}
H_L	Latent surface heat flux*	W m^{-2}
H	Total surface heat flux ($H_S + H_L$)	W m^{-2}
SST	Sea surface temperature*	°C
wspd10	10-m horizontal wind speed*	m s^{-1}

d. *Computation of vertical accelerations along trajectories*

Parcel vertical accelerations $(Dw/Dt) = (\partial w/\partial t) + u(\partial w/\partial x) + v(dw/dy) + w(\partial w/\partial z)$ along backward trajectories are computed using 1-min centered time differences of w previously smoothed using a 2-min running mean.[4] The anelastic vertical momentum equation can be written as (Houze 1993, p. 36; Braun 2002; Fierro et al. 2012)

$$\frac{Dw}{Dt} \approx \underbrace{-\frac{1}{\overline{\rho}}\frac{\partial p'}{\partial z}}_{\mathrm{PGA}} + \underbrace{g\left[\frac{\theta'_v}{\overline{\theta_v}} + (\kappa-1)\frac{p'}{\overline{p}} - q'_{\mathrm{HYD}}\right]}_{\mathrm{BA}} + \text{mixing}, \tag{5}$$

where overbars (primes) denote horizontal averages over (perturbations from) a hydrostatic height-dependent horizontal base state, g is the gravitational constant, $\kappa = 0.286$, and other symbols are defined in Tables 1 and 2. From left to right, the Eq. (5) forcing terms on Dw/Dt are the vertical perturbation pressure gradient acceleration (PGA), buoyant acceleration (BA), and subgrid-scale turbulent momentum mixing. The BA can be decomposed into three components: (i) thermal buoyancy $g(\theta'_v/\overline{\theta_v})$, (ii) a "pressure-buoyancy term" $g(\kappa-1)(p'/\overline{p})$ that absorbs p' contributions to ρ', and (iii) hydrometeor loading gq'_{HYD}. Vertical acceleration profiles are generated for MBL-origin trajectories seeded over the 16:00–18:00 period using the methods described in section 2c, except that trajectory output is binned over smaller 100 m, as opposed to 250 m, vertical intervals to minimize the residual difference between parcel Dw/Dt and its forcing terms. Figure 2b shows the number of trajectories from each subsample used for computing vertical acceleration statistics at each 100-m bin.[5]

Previous studies have used different basic-state definitions when computing the Eq. (5) right-hand terms from model output because of no unique definition of buoyancy (Zhang et al. 2000; Braun 2002; Fierro et al. 2012). Here, the hydrostatic base states for p, θ_v, and q_{HYD} are defined in cylindrical (r, λ, z) coordinates as their respective horizontal averages over the 180° azimuthal arc centered on the parcel:

$$\overline{\theta_v}(r,\lambda,z,t) = \frac{\sum_{j=\lambda-90}^{j=\lambda+90} \theta_v(r,j,z,t)}{n_j}, \tag{6}$$

where λ is measured in degrees counterclockwise and $n_j = 181$ points are used in the azimuthal sum. Following Braun (2002), our base state definition excludes nearby air radially inside (outside) of the parcel because we expect this air to be warmer (cooler) than the parcel due to Wilma's warm core structure. As in Braun (2002), the base state hydrometeor mixing ratio is excluded from Eq. (5) since it contributes to hydrostatic balance between $\overline{\theta_v}$ and $\overline{p}$. Unlike our present study, Braun (2002) defined the base state for a given field as its combined wavenumber-0 and wavenumber-1 components following a Fourier decomposition. Our choice of a parcel-centered 180° azimuthal running mean was based on our expectation that such an arc should be sufficiently long for v_t and θ_v averaged along it to remain in thermal wind balance. We also computed the left- and right-hand sides of Eq. (5) along a selected trajectory running through a CB core using a series of base state arc lengths, ranging from 16° to 360°. Although we found very similar results for arc lengths ≥ 120°, increasing disagreements between

[4] Smoothing trajectory output w in this manner improves the agreement between the left and right-hand sides of Eq. (5), presumably because it helps smooth out spurious parcel w tendencies resulting from errors in the spatiotemporal interpolation of parcel winds from the model grid.

[5] Statistics for all diagnostic variables other than the Eq. (5) terms use the full MBL-origin sample. The relatively large computational expense incurred from computing the hydrostatic base state at all trajectory positions motivated use of the smaller trajectory sample size for vertical momentum budgets.

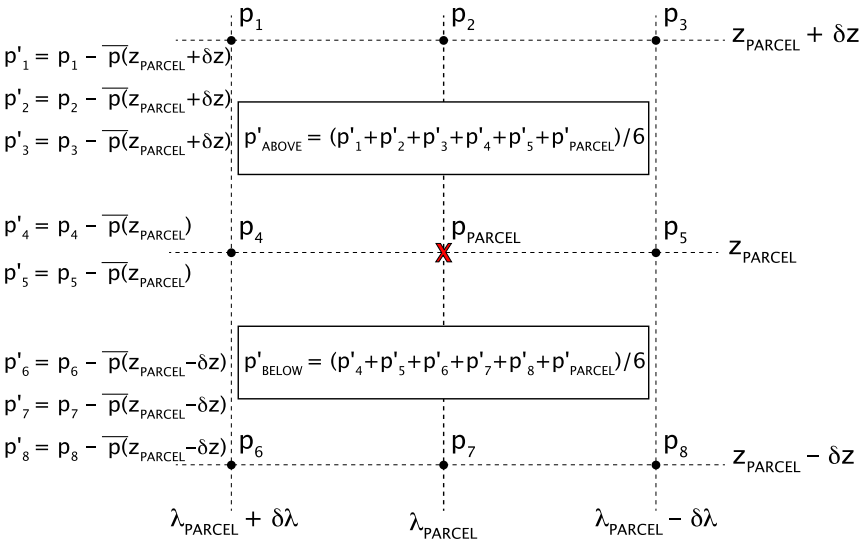

FIG. 3. Schematic illustrating the numerical technique used for computing the PGA. For a given parcel at coordinates (r_{PARCEL}, $\lambda_{\mathrm{PARCEL}}$, z_{PARCEL}), perturbation pressures p'_{ABOVE} and p'_{BELOW} are computed as six-gridpoint averages over the ±1° arc surrounding $\lambda_{\mathrm{PARCEL}}$ and the vertical layer of thickness $\delta z = 500$ m above and below z_{PARCEL}, respectively. Overbars denote basic state pressures computed using Eq. (6) and p symbols denote local pressure values at grid points identified by subscripts. Therefore, $p'_{\mathrm{ABOVE}} = (p'_1 + p'_2 + p'_3 + p'_4 + p'_5 + p'_{\mathrm{PARCEL}})/6$ and $p'_{\mathrm{BELOW}} = (p'_4 + p'_5 + p'_6 + p'_7 + p'_8 + p'_{\mathrm{PARCEL}})/6$.

the Dw/Dt and PGA + BA profiles become evident for smaller arc lengths, especially in the upper troposphere (not shown).

The Fig. 3 schematic summarizes the numerical method used for computing the PGA along trajectories. First, hydrostatic base state pressures are defined using Eq. (6) applied to the pressure field at heights $z \pm \delta z$ relative to the parcel (r, λ, z) position, where $\delta z = 500$ m. Next, perturbation pressures p'_{ABOVE} and p'_{BELOW} are computed as the local p' averaged over a 2° arc centered on the parcel over the z to $z + \delta z$ and z to $z - \delta z$ layers, respectively. Finally, we compute PGA $= (p'_{\mathrm{ABOVE}} - p'_{\mathrm{BELOW}})/\overline{\rho}\delta z$.

e. *Updraft element definition and entrainment analysis*

It is important that we distinguish between updraft trajectory parcels and larger "updraft elements," where the latter contain numerous adjacent parcels with varying thermodynamic properties. Here we follow Jorgensen et al. (1985) and define an updraft element as the region surrounding trajectory positions where w exceeds 0.5 m s^{-1} and RH exceeds 95%. To maintain consistency with CZ13 and M15, we define CBs as updraft elements containing at least one gridpoint above $z = 11$ km with $w \geq 15$ m s^{-1}.

Previous theoretical and idealized modeling studies have identified two basic processes driving the entrainment of environmental air into cloudy updrafts: (i) turbulent mixing across the updraft outer edge, and (ii) local[6] radial inflow into the updraft element as required by mass continuity to balance the updraft acceleration (i.e., "dynamic entrainment") (Houze 1993; Morrison 2017). Rather than attempt to quantify mass exchange rates resulting from dynamic and turbulent mixing, we instead define three variables along trajectories that should influence Lagrangian θ_e tendencies caused by mixing with air originating outside of the updraft element, as shown schematically in Fig. 4: (i) d_{EDGE}—the smallest distance in any Cardinal direction to the updraft element boundary, (ii) D_{AVG}—the mean updraft element diameter, and (iii) $\theta_{e,\mathrm{ENV}}$—θ_e horizontally averaged over the local environment. Herein the environment for any trajectory is defined as a six-gridpoint line extending outward from d_{EDGE}.

3. Analysis of convective burst structure and thermodynamics

We begin by examining the time evolution of CB updraft element "CB-E1," shown in Fig. 1 near its peak

[6] We use the term "local" here to describe lateral inflow into the updraft core driven by convective-scale mass continuity, which is different from the vortex-scale radial inflow that constitutes a portion of the TC secondary circulation.

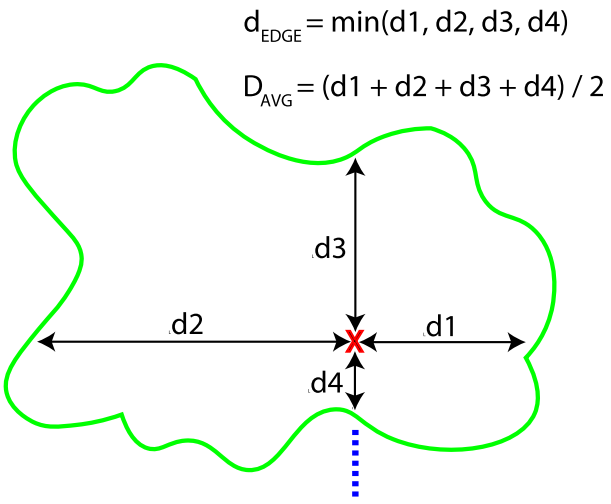

FIG. 4. Schematic showing the basic parameters used to study the impacts of entrainment on trajectory updrafts. The green curve marks the outer boundary of the local updraft element, defined by $w > 0.5$ m s^{-1} and relative humidity > 95%. Distances d1, d2, d3, and d4 are measured in the four cardinal directions from the parcel position, denoted by the red "X" symbol, to the updraft element boundary. Symbols "d_{EDGE}" and "D_{AVG}" denote the smallest distance in any cardinal direction to the updraft element boundary and the mean updraft element diameter, respectively. Environmental θ_e ($\theta_{e,\mathrm{ENV}}$) is averaged along the blue dashed line segment.

intensity at WRF prediction time 16:10. In the upper troposphere, the updraft is roughly 10 km wide and surrounded by downdrafts, the latter having peak $|w| > 5$ m s^{-1} (Fig. 1a). The northwestward-directed subsidence originates near the tropopause, roughly denoted by the 375-K isentrope (Fig. 1b), and it may contribute to the development of Wilma's upper-level warm core provided that adiabatic warming in the downdraft outweighs diabatic cooling (Zhang and Chen 2012; CZ13; M15). A vertical cross section taken through CB-E1 reveals a ~3-km-wide core of extreme w exceeding 30 m s^{-1} in the z = 10–14-km layer (Fig. 1b). The local potential temperature θ anomaly collocated with the updraft core may result from LHR exceeding adiabatic cooling. High-resolution airborne Doppler radar-derived analyses of CBs in other TCs have captured similar features, namely, intense $w > 15$ m s^{-1} peaking in the upper troposphere with ~10-km updraft element width, and downdrafts flanking the updraft element (Guimond et al. 2010, 2016).

a. Three-dimensional trajectory

To better understand the thermodynamics contributing to the extreme w found in Wilma's CB cores, let us follow the history of a parcel that passes through CB-E1 at 16:10, identified herein as Trajectory-CB. Figures 5a and 5b show its three-dimensional path, beginning in the MBL at t = 14:00, and ending at its z = 14 km, t = 18:00 seed position. Between 14:00 and 15:40, the parcel remains in the MBL while spiraling cyclonically inward. After 15:40, Trajectory-CB accelerates upward monotonically, completing just one-half circle transit around the western and southern eyewall before achieving its 30.6 m s^{-1} w_{MAX} around z = 13 km, t = 16:10. By comparison, Trajectory-SC, which leaves the MBL at a similar time but is more representative of the background secondary circulation with w_{MAX} = 8.9 m s^{-1}, completes one and a half loops around the eyewall during ascent to z = 14 km (Figs. 5c,d). Returning to Trajectory-CB, we find a rapid upward deceleration after 16:10; by 16:15 its w approaches zero at z ~15.5 km. Thereafter the parcel translates cyclonically around the upper-level eyewall (Figs. 5a,b) while its w oscillates roughly sinusoidally between ±2 m s^{-1} with a ~45-min period (not shown)—possibly forced by convectively generated gravity waves. One notable exception is a 5-min window after 16:39 when the parcel executes a sharp anticyclonic loop while descending from a z ~ 17.5-km peak height (Figs. 5a,b) that it reaches after having been lofted by a 4 m s^{-1} updraft (not shown).

b. Parcel θ_e evolution

A parcel's θ_e is conserved under inviscid pseudoadiabatic ascent; however, for real TC updrafts it is not strictly conserved because Lagrangian θ_e sources and sinks include the latent heat of fusion, cloud–radiative interactions, mixing, and ocean surface heat fluxes (Bolton 1980; Zhang et al. 2002). While transiting the MBL between 14:00 and 15:40, Trajectory-CB experiences a 2.96-K θ_e increase. This agrees closely with the 2.79-K $\Delta\theta_e$ value predicted by Liu et al. (1999) to result from upward ocean surface sensible and latent heat fluxes, using the parcel $\overline{\theta_e}$, $\overline{T}$, $\overline{p}$, ΔT, Δp, and Δq_v from 14:00 to 15:40 (see their footnote 1). Notably, the Trajectory-CB parcel moves over locally maximized ocean surface heat fluxes around 15:00 (Figs. 5a,b). In section 4b we will revisit the question of whether CB parcels, on average, experience higher ocean surface heat fluxes compared to the background secondary circulation prior to ascent.

When the Trajectory-CB parcel ascends out of the MBL at 15:40, we find it, as indicated by a black triangle in Figs. 6a and 6b, on the northwestern edge of a band-shaped low-level updraft element, hereafter "E0," that is collocated with enhanced radial inflow convergence in Wilma's western eyewall. Similarly, Hazelton et al. (2017) found that CBs tended to originate from regions with locally enhanced low-level convergence in their simulations of Hurricanes Dean (2007) and Bill (2009). Meanwhile, the Trajectory-SC parcel, shown as a black dot in Figs. 6a and 6b, is near z ~ 900 m and roughly

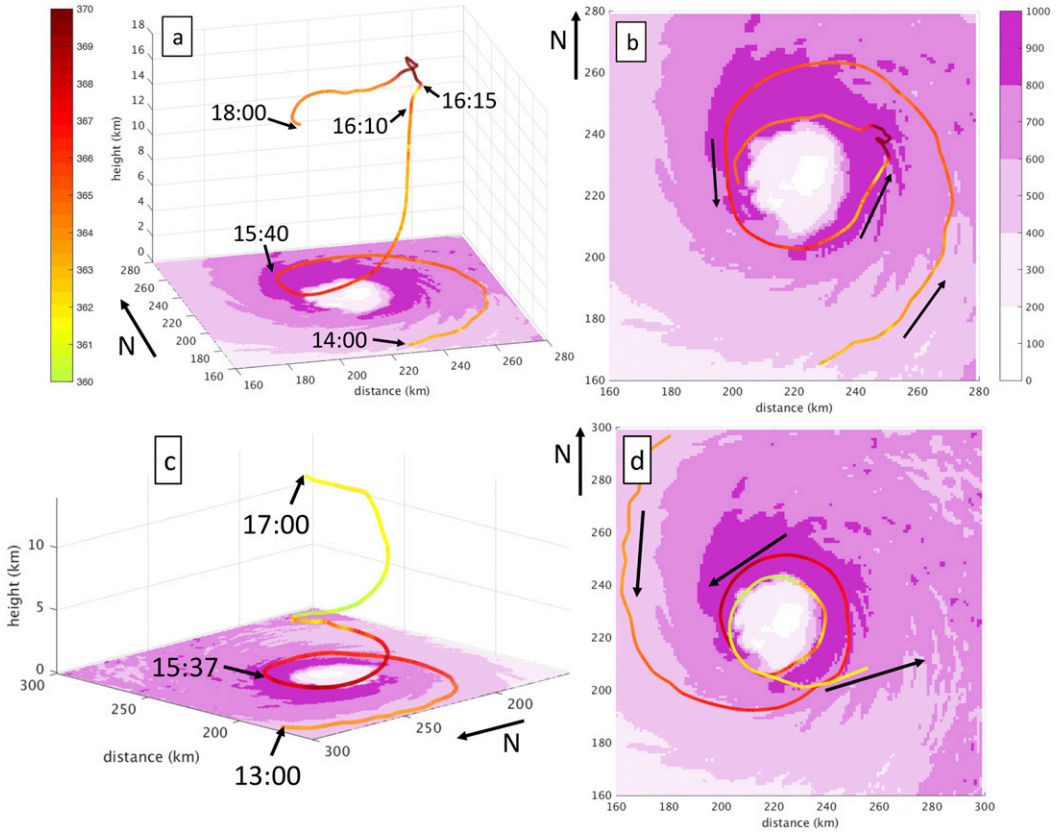

FIG. 5. (a) Three-dimensional and (b) x–y planar projection of Trajectory-CB, color coded by parcel θ_e (K). WRF prediction times (hh:mm format) for selected points along the trajectory described in the text are also shown in (a), with arrows in (b) pointing in the direction of parcel movement in WRF Model time. Purple shading denotes the sum of latent and sensible ocean surface heat fluxes (W m^{-2}) at 15:00. (c),(d) As in (a) and (b), but for Trajectory-SC.

45° cyclonically downwind of the Trajectory-CB parcel. Figures 7 and 8 show azimuth–height cross sections X1 and X2 that are slanted outward to approximately align with r–z planar projections of Trajectory-CB and Trajectory-SC, respectively. The portion of E0 intersecting X1 near Trajectory-CB's 15:40 location is collocated with a column of locally higher θ_e air extending from the MBL upward to $z \sim 2.5$ km (Fig. 7a).[7] Figure 8a confirms that the Trajectory-SC parcel is also currently embedded in E0. At 15:40, most columns in these two cross sections exhibit potentially unstable conditions (i.e., with θ_e rapidly decreasing above the MBL, reaching a minimum around $z = 4$ km, and increasing with height above; Figs. 7a and 8a). Other modeling studies have documented a midtropospheric θ_e minimum in a TC's surroundings that extends into the outer eyewall (Liu et al. 1999; Braun 2002).

Trajectory-CB θ_e decreases from 366 to 363 K over the next 25 min while the parcel ascends to $z = 6$ km (Fig. 5a). By contrast, Trajectory-SC takes 40 min to reach $z = 6$ km while its θ_e decreases from 368 to 360 K (Fig. 5c). Over these two respective periods (i.e., 15:40–16:05 and 15:40–16:20), both parcels rotate cyclonically with phase speeds close to the 35.6° $(5\ \text{min})^{-1}$ mean angular velocity obtained by averaging v_t in X1 over $\lambda = 120°$–360°, $z = 0$–6 km, $t = 15{:}40$–16:05 while remaining embedded within a cluster of updraft elements E1, E2, and E3 that develop out of E0 (Figs. 6a,c, 7a–e, and 8a–d). After 15:50, the Trajectory-CB parcel ascends through a high θ_e anomaly associated with element E1 that grows upward through the midtroposphere while remaining rooted in the MBL (Figs. 7c,d). In some aspects, the evolution of E1 resembles Morton et al. (1956)'s analytical model of a plume growing above a steady buoyancy source

[7] The azimuthal–height cross section shown in Fig. 7a is taken several kilometers radially inside of the Trajectory-CB location at 15:40; however, the parcel is still moving radially inward at this time. By 15:45, the parcel has moved inside the 2-km-wide region used for averaging the variables shown in Figs. 7b–f (not shown).

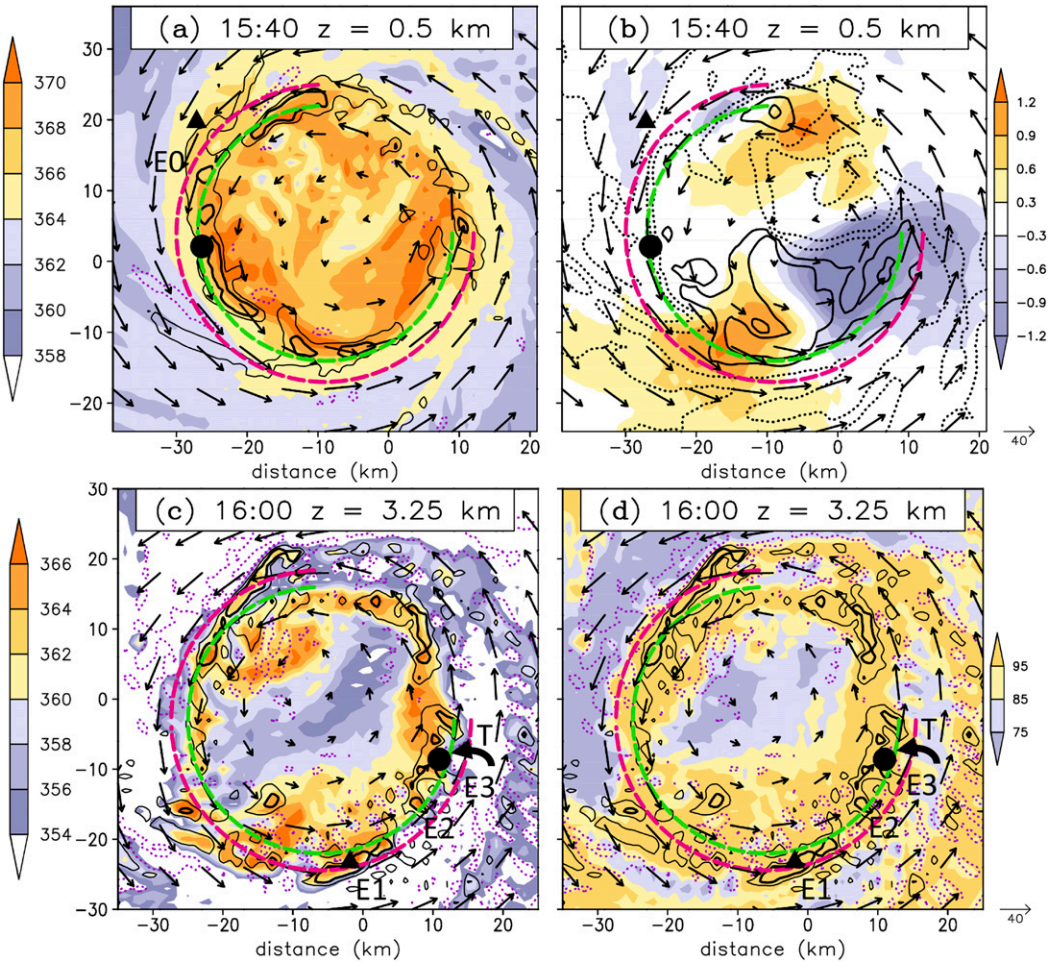

FIG. 6. (a) WRF-predicted t = 15:40 and z = 0.5-km θ_e (shaded; K), horizontal storm-relative flow vectors (m s^{-1}) and vertical velocity w (black contoured for 1 and 2 m s^{-1}; purple dotted contoured for −1 m s^{-1}). (b) As in (a), but with the z = 0.5-km p' field (shaded; hPa) and radial winds (solid black contoured for 2, 5, and 10 m s^{-1}; dotted black contoured for −10, −5, and −2 m s^{-1}). (c) As in (a), but for t = 16:00 and z = 3.25 km. In (c), w is thin-black (thick-black) contoured for 2 (5) m s^{-1} and purple-dotted contoured for −3 and −1 m s^{-1}. (d) As in (c), but with relative humidity (shaded; %) in lieu of θ_e. The black triangle denotes the Trajectory-CB (x, y) coordinates when located at (z = 0.45 km, t = 15:40) and at (z = 3.27 km; t = 16:00). The black closed circle denotes the Trajectory-SC (x, y) coordinates when located at (z = 0.91 km; t = 15:40) and at (z = 3.37 km; t = 16:00). Dashed magenta (green) arc denotes the intersection of the horizontal plane with the azimuthal–height section X1 (X2) shown in Fig. 7 (Fig. 8). Letter labels E0, E1, E2, and E3 denote updraft elements discussed in the text. The letter label T in (c) and (d) as well as its associated thick black arrow shows the low-θ_e tongue region impinging on the eyewall near E3.

(Morrison 2017). Therefore, it appears that parcels rising out of E1 over the 15:50–16:00 period have built a higher-θ_e ''tunnel'' that could limit environmental air entrainment into the Trajectory-CB parcel once it takes its turn to ascend. By contrast, the significantly greater θ_e reduction experienced by the Trajectory-SC parcel while ascending through the lower-to-middle troposphere likely results from entraining lower-θ_e environmental air. Trajectory-SC remains near the cyclonically downwind edge of E3, adjacent to a low-θ_e tongue ''T'' that contains embedded downdrafts and subsaturated air wrapping into the eyewall from outer regions (Figs. 6c,d and 8b,c).

E1 explosively intensifies between 16:00 and 16:05, particularly in the upper troposphere where peak w increases from <5 to >25 m s^{-1} (Figs. 7e,f). It has now become a mature CB, hereafter named CB-E1. At 16:05 it extends from near the top of the MBL to above z = 16 km, tilting cyclonically downwind below z = 8 km and becoming vertically upright for higher levels (Fig. 7e). Over the next 5 min as CB-E1 approaches its peak intensity, the height of maximum w

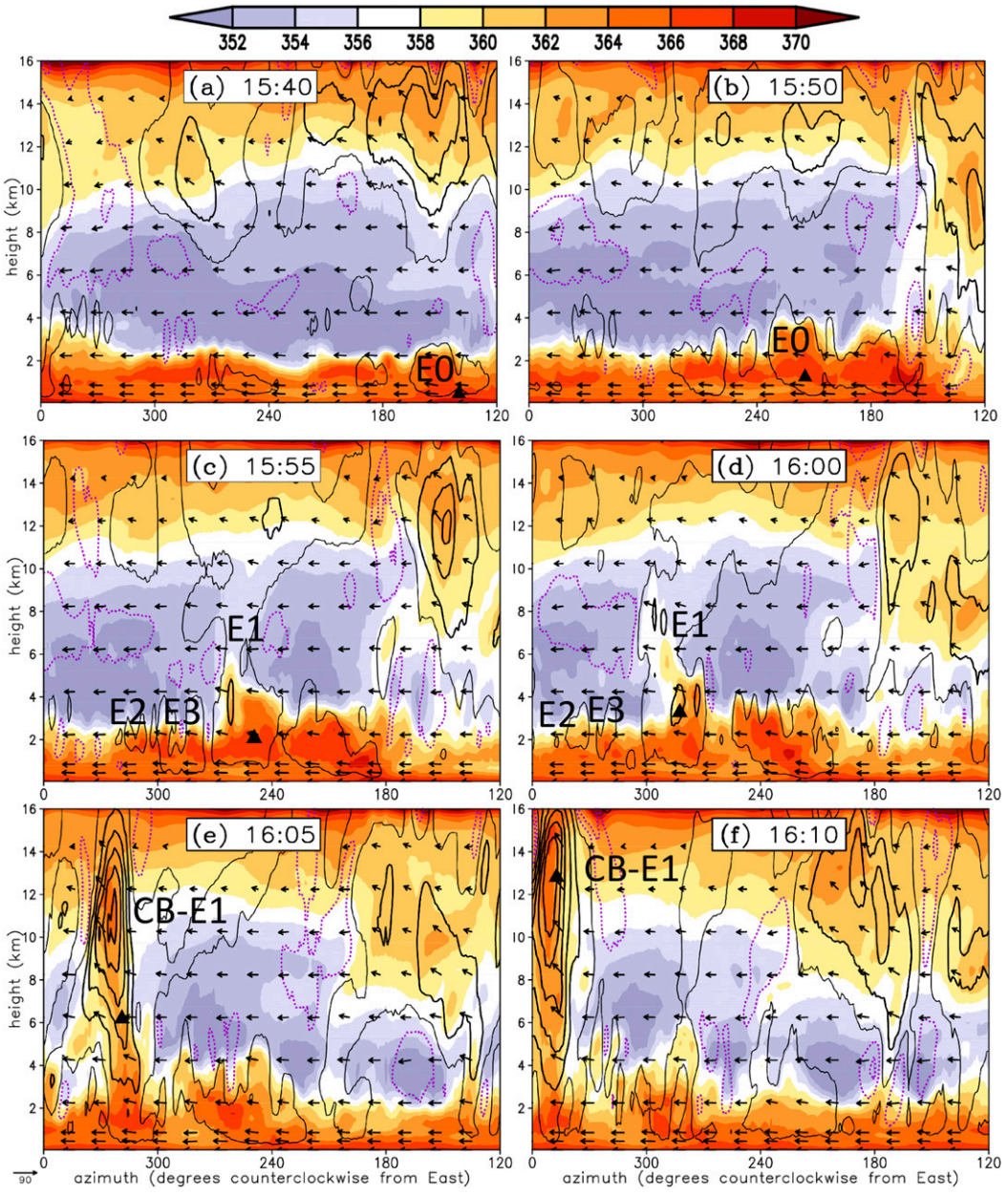

FIG. 7. (a) Azimuth–height cross section of WRF-predicted θ_e (shaded; K) and w (thin black contour for 1 m s^{-1}; thick black contours for 5, 10, 15, 20, 25, and 30 m s^{-1}; purple dotted contours for -1 and -3 m s^{-1}) with in-plane flow vectors (m s^{-1}; vertical motions multiplied by 3) at 15:40. (b)–(f) As in (a), but for WRF prediction times 15:50, 15:55, 16:00, 16:05, and 16:10, respectively. All cross sections shown here are taken along the conical surface X1 that slopes outward from $r = 21$ km, $z = 1$ km to $r = 24$ km, $z = 15$ km, and all variables shown here are averaged over a 2-km-wide radial band centered on X1. The black triangle marks the position of Trajectory-CB. Letter labels E0, E1, E2, E3, and CB-E1 denote updraft elements discussed in the text.

shifts upward from $z \sim 11$ km to $z \sim 13$ km while CB-E1 becomes more vertically aligned through the entire troposphere—perhaps a consequence of the lower (upper) portion being advected cyclonically downwind by a stronger (weaker) layer-mean v_t (Figs. 7e,f). The Trajectory-CB parcel accelerates upward through CB-E1's core between 16:05 and 16:10, ascending from $z = 6$ km to $z = 13$ km (Figs. 7e,f). This parcel's θ_e increases by ~1 K over this period, likely due to a combination of (i) latent heating of fusion from ice-phase

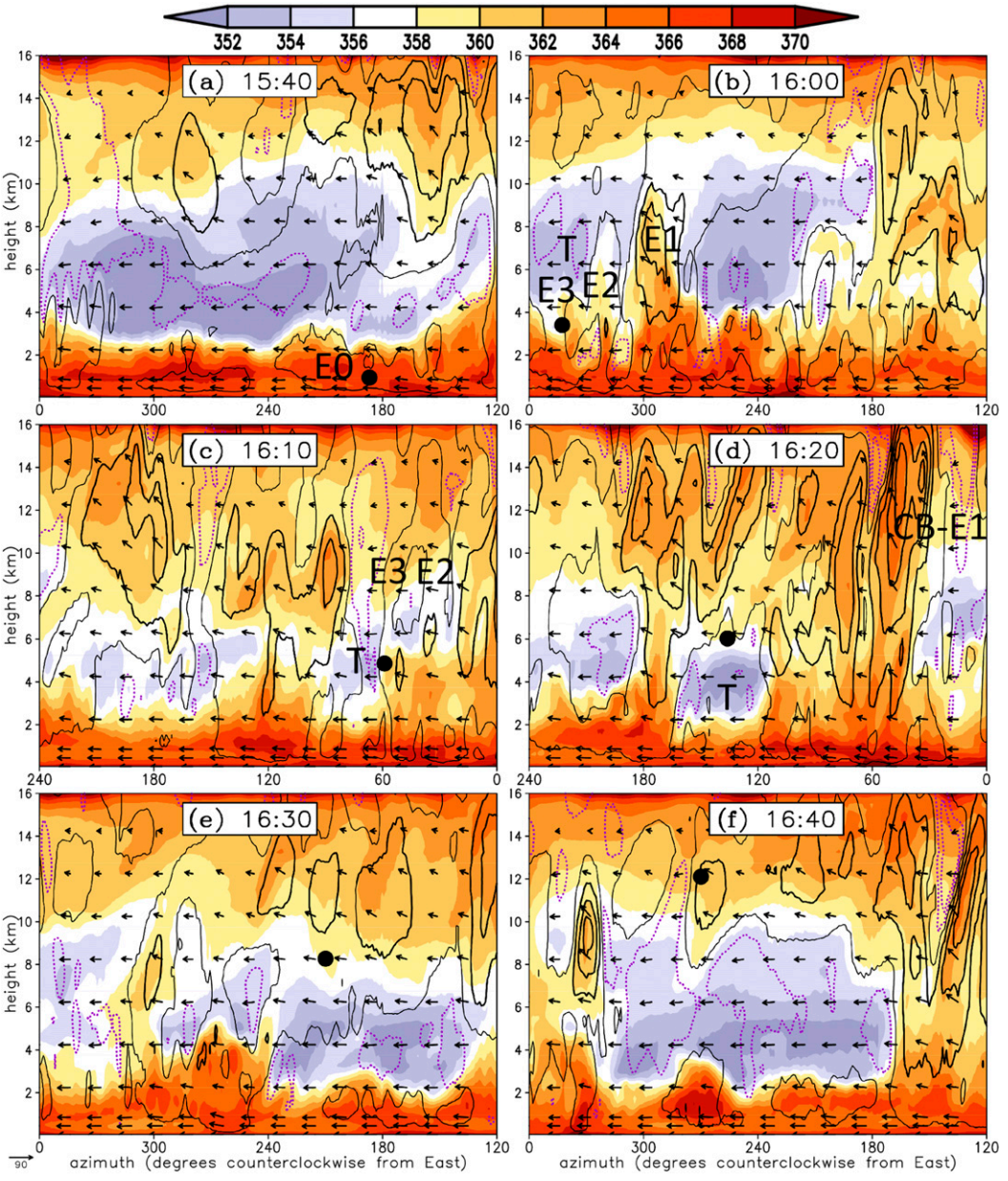

FIG. 8. As in Fig. 7, but for (a) 15:40, (b) 16:00, (c) 16:10, (d) 16:20, (e) 16:30, and (f) 16:40. Here all cross sections are taken along the conical surface X2 that slopes outward from $r = 18$ km, $z = 1$ km to $r = 23.5$ km, $z = 13$ km. The black closed circle marks the position of Trajectory-SC. Letter labels E0, E1, E2, E3, and CB-E1 denote updraft elements discussed in the text. The letter label T denotes the low-θ_e tongue also discussed in the text. Note the different azimuthal ranges shown in (c) and (d) compared to (a), (b), (e), and (f).

microphysical processes (Fierro et al. 2012; M15); and (ii) mixing with higher-θ_e air previously warmed by fusion LHR in other parcels (Figs. 7e,f).

By 16:20 Trajectory-SC has almost ''cleared the hurdle'' in terms of its avoiding transit through the core of low-θ_e region T and its associated downdrafts (Fig. 8d). Ten minutes later it has gained another 2 km in altitude while transiting through a portion of the upper-tropospheric eyewall characterized by modest ascent (Fig. 8e). By 16:40 Trajectory-SC has reached $z \sim 12$ km while rising through an embedded core of enhanced w (Fig. 8f).

c. *Parcel vertical momentum budget*

The positive θ_e anomaly inside the intensifying CB-E1 relative to nearby areas at the same height (Figs. 7a–f)

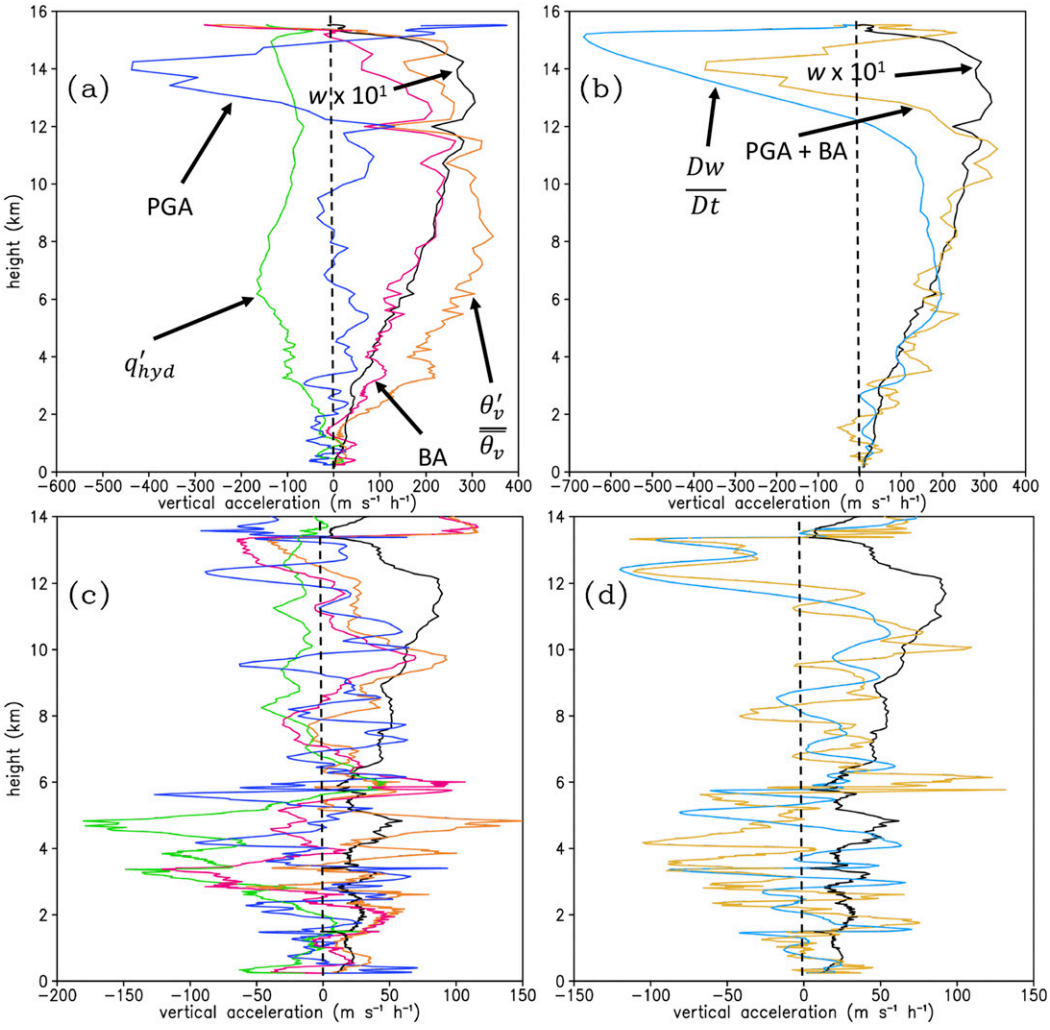

FIG. 9. (a) Buoyant acceleration (BA; $m^{-1}\,s^{-1}\,h^{-1}$; magenta line), with its thermal ($m^{-1}\,s^{-1}\,h^{-1}$; orange line) and hydrometeor loading ($m^{-1}\,s^{-1}\,h^{-1}$; green line) components, vertical perturbation pressure gradient acceleration (PGA; $m^{-1}\,s^{-1}\,h^{-1}$; blue line), and w ($\times 10$ m s^{-1}; black line), all plotted as a function of height along a portion of Trajectory-CB. (b) As in (a), but with vertical acceleration Dw/Dt ($m^{-1}\,s^{-1}\,h^{-1}$; light-blue line) and the sum of the BA and PGA (m $s^{-1}\,h^{-1}$; light-orange line). (c),(d) As in (a) and (b), but for Trajectory-SC. Note the different magnitudes of the budget terms between the two trajectories [cf. the horizontal axes between (a) and (c) and between (b) and (d)].

suggests that the aggregate mass of parcels comprising CB-E1 is thermally buoyant relative to the hydrostatic base state (section 2d) and experiences upward acceleration. To confirm this, and to better understand the relative impacts of hydrometeor loading and the PGA, we now compute vertical acceleration terms from Eq. (5) along Trajectory-CB, with a focus on the period of continuous parcel ascent through the $z = 0.25$–15.5-km layer.

Figure 9a shows vertical profiles along Trajectory-CB of w, BA, PGA, as well as the thermal [$g(\theta'_v/\overline{\theta_v})$] and hydrometeor loading (gq'_{HYD}) contributions to the BA. We find a positive BA that increases nearly monotonically with height from the upper MBL ($z = 0.25$–0.5 km) to a maximum value of ~250 m $s^{-1}\,h^{-1}$ near $z = 11.5$ km except for a brief dip below zero around $z = 1.5$ km. The Eq. (5) $g(\kappa - 1)(p'/\overline{p})$ term (not shown) is positive and similar in magnitude to $g(\theta'_v/\overline{\theta_v})$ below $z = 1.5$ km–consistent with the parcel originating from a region of negative low-level p' (Fig. 6b), whereas for higher levels it becomes from one to two orders of magnitude smaller than $g(\theta'_v/\overline{\theta_v})$. Although the $g(\theta'_v/\overline{\theta_v})$ and gq'_{HYD} terms are comparably large within an order of magnitude, the downward-directed hydrometeor loading is insufficient to offset the very large thermal buoyancy anywhere between $z = 2$ km and $z = 15$ km. Two positive BA spikes near $z = 0.4$ and $z = 0.9$ km, resulting from

nearly equal $\sim+15$ m s^{-1} h^{-1} contributions from $g(\theta_v'/\overline{\theta_v})$, $g(\kappa-1)(p'/\overline{p})$, and $gq_{\rm HYD}'$, appear to have lifted the parcel out of the MBL, given the generally negative PGA below $z = 2$ km. Between $z = 3$ km and $z = 12.5$ km, the PGA is alternately positive and negative while remaining significantly weaker than the BA. Note, however, the sharp negative PGA spike in the upper troposphere, which we shall examine shortly. Figure 9b shows that the sum BA + PGA is in generally good agreement with Dw/Dt; the lower WRF vertical resolution in the upper troposphere (CZ11) may partially explain the greater residual above $z = 8$ km between the left- and right-hand sides of Eq. (5), excluding the mixing term.

To better understand the physical origins of the Trajectory-CB vertical acceleration terms, let us examine the distribution of θ_v', $q_{\rm HYD}'$, and p' in an azimuthal–height cross section through CB-E1 and its environment, shown in Fig. 10. The large positive θ_v' and $q_{\rm HYD}'$, collocated with the mid-to-upper level CB-E1 core (Figs. 10a,b), clearly suggest that LHR from condensation and fusion generates the positive deep-layer thermal buoyancy responsible for the parcel's extreme $w_{\rm MAX}$ (Fig. 9a). Unfortunately, microphysical heating tendency output variables are not available for this WRF prediction, and therefore we cannot further study the relative contributions of liquid-phase (i.e., condensation) and ice-phase (i.e., freezing, riming, and deposition) processes toward parcel θ_v'.

Our finding of a comparatively weak PGA through much of this parcel's ascent differs from Braun (2002), who computed an upward PGA that offset a downward BA within the MBL and a downward PGA that nearly offset an upward BA above the MBL along a trajectory rising through simulated Hurricane Bob's (1991) eyewall (see his Fig. 17). Idealized simulations of upright nonrotating buoyant updrafts predict a downward-directed PGA opposing the BA (Markowski and Richardson 2010; Morrison 2016), provided that VWS—and therefore dynamic contributions to the p' field—is small. Conceptually, this can be understood from a mass continuity perspective, where a positive p' at the updraft top is needed to push surrounding air laterally outward and a negative p' at the updraft bottom is needed to draw surrounding air inward to fill its wake. Using similar assumptions, Morrison (2016) developed an analytical updraft model in which the downward PGA magnitude is proportional to the updraft width–height ratio; thus, it is possible that CB-E1's deep vertical extent, together with its cyclonic downwind vertical tilt below $z = 10$ km (Fig. 10c), may have helped keep the PGA relatively weak below $z = 12.5$ km (Fig. 9a). Nevertheless, a p' field consistent with Morrison's (2016) analytical model surrounds the CB-E1 $w > 25$ m s^{-1} core, with positive

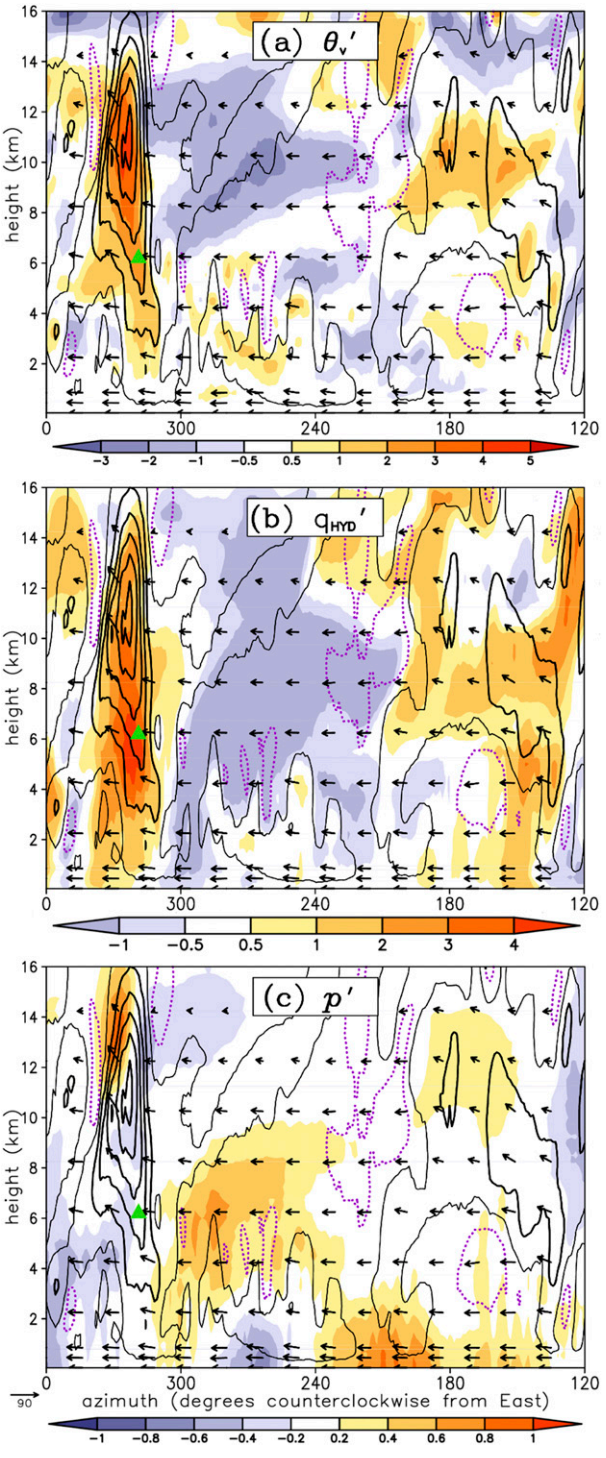

FIG. 10. (a) As in Fig. 7, but for WRF prediction time 16:05, with perturbation virtual potential temperature θ_v' (shaded; K). (b) As in (a), but with perturbation total hydrometeor mixing ratio $q_{\rm HYD}'$ (shaded; g kg^{-1}). (c) As in (a), but with perturbation pressure p (shaded; hPa). All perturbation variables shown here are defined with respect to the hydrostatic base state (section 2d). The green triangle denotes the position of Trajectory-CB.

(negative) p' above (below) it (Fig. 10c). This local p' couplet generates the strongly negative PGA over the z = 12.5–15-km layer (confirmed by replotting Fig. 10c for 1610 UTC, not shown) that forces rapid vertical deceleration of the Trajectory-CB parcel (Figs. 9a,b). The positive p' anomaly found above and cyclonically downwind of CB-E1 (Fig. 10c) resembles the "meso-high" structures observed above mesoscale convective systems (Fritsch and Maddox 1981), albeit on a smaller scale. It may be hydrostatically forced by a cold anomaly directly above it (Fig. 10a), with the latter likely generated by adiabatic cooling in parcels overshooting the equilibrium level. Dynamic contributions to the p' field around CB-E1 may also result from the interaction of the updraft with the horizontal (Zhang et al. 2000) and vertical (Rotunno and Klemp 1982) shear of v_t, and they could be examined in a future study.

By contrast, the Trajectory-SC w profile has two significant maxima, with one peak of ~5 m s^{-1} near z = 5 km and another peak of ~9 m s^{-1} near z = 12 km (Fig. 9c). Comparing its vertical acceleration terms in the upper MBL (z = 0.25–0.5 km) with those of Trajectory-CB, we find a similarly weak positive $g(\theta_v'/\overline{\theta_v})$. However, unlike for Trajectory-CB, $gq_{\rm HYD}'$ is negative and PGA is positive[8] in the upper MBL (cf. Figs. 9a,c), consistent with Trajectory-SC departing the MBL in a more heavily precipitating region (not shown). Over the z = 0.5–5-km layer, thermal buoyancy is positive but considerably weaker than that of Trajectory-CB. Trajectory-SC's BA becomes negative over the z = 3–5.5-km layer due to $g(\theta_v'/\overline{\theta_v})$ being unable to offset $gq_{\rm HYD}'$, which helps decelerate parcel w to near zero around z = 6 km (Fig. 9c). The recovery of upward motion at higher levels likely results from a combination of (i) rapid hydrometeor unloading, (ii) fusion LHR—note the positive $g(\theta_v'/\overline{\theta_v})$ in the z = 8–12-km layer, and (iii) a mesoscale environment characterized by ascent (Figs. 8e,f). Previous modeling studies (Fierro et al. 2009, 2012; Wang 2014; M15) and observations (Hildebrand et al. 1996; May and Rajopadhyaya 1996) have also found bimodal w profiles with midlevel minima in tropical oceanic convective updrafts. The left- and right-hand sides of Eq. (5) show fairly good agreement for this parcel at most heights (Fig. 9d).

4. Trajectory updraft statistics

Let us now investigate the general characteristics of Wilma's $w_{\rm MAX}$-Extreme parcels in an attempt to better understand how they become differentiated from the background secondary circulation. To accomplish this, we stratify all 43 347 MBL-origin backward trajectories by $w_{\rm MAX}$ into five subsamples per the procedure described in section 2c and then compare statistics derived from the different subsamples.

a. General thermodynamic and microphysical characteristics

Figure 11a shows $\overline{w_{360}'}^{S}(k)$ profiles for $w_{\rm MAX}$-8, $w_{\rm MAX}$-12, $w_{\rm MAX}$-16, $w_{\rm MAX}$-20, and $w_{\rm MAX}$-Extreme, where $w_{360,i}'(k)$ is the perturbation from azimuthally averaged $w(r, z, t)$ along the ith trajectory, averaged over 250-m layer k, and the overbar with the "S" superscript denotes an average over all trajectories in the subsample. Figure 11a also shows that $w_{\rm MAX}$-12 contains the largest fraction, ~45%, of all MBL-origin updrafts, and we shall hereafter consider it most representative of the background secondary circulation. Above z = 3 km, $\overline{w_{360}'}^{S}(k)$ becomes larger with increasing subsample $w_{\rm MAX}$. The $w_{\rm MAX}$-16, $w_{\rm MAX}$-20, and $w_{\rm MAX}$-Extreme $\overline{w_{360}'}^{S}(k)$ profiles are all unimodal with upper-tropospheric maxima, consistent with the M15 cumulative contoured frequency by altitude diagram (CCFAD) analysis of Wilma's early RI period (see their Fig. 8a). In contrast, the $w_{\rm MAX}$-8 and $w_{\rm MAX}$-12 $\overline{w_{360}'}^{S}(k)$ profiles have a rather flat and weakly bimodal appearance (Fig. 11a).

The $w_{\rm MAX}$-16, $w_{\rm MAX}$-20 and $w_{\rm MAX}$-Extreme $\overline{\theta_{v,360}'}^{S}(k)$ profiles have similar shapes to their $\overline{w_{360}'}^{S}(k)$ profiles, peaking in the upper troposphere at 0.8, 1.3, and 2.0 K, respectively—about 1 km below their respective maxima in $\overline{w_{360}'}^{S}(k)$ (Fig. 11b). The $w_{\rm MAX}$-8 and $w_{\rm MAX}$-12 $\overline{\theta_{v,360}'}^{S}(k)$ profiles are flatter and peak near 0.5 K just below the melting level. Supercooled liquid water mixing ratios $\overline{q_{\rm LIQ}'}^{S}(k)$ increase with $w_{\rm MAX}$ above the melting level (Fig. 11c), which is not surprising since stronger updrafts at these heights (Fig. 11a) more strongly counteract the fallout of liquid hydrometeors generated by warm-rain processes below. Frozen hydrometer mixing ratios $\overline{q_{\rm FRZ}'}^{S}(k)$, on the other hand, show a more complex dependency on $w_{\rm MAX}$ (Fig. 11d). All subsamples except for $w_{\rm MAX}$-8 show a lower peak roughly 1–2 km above the melting level, associated with graupel (confirmed by plotting subsample-mean graupel profiles, not shown), that becomes sharper with increasing $w_{\rm MAX}$. The upper peak above z = 8 km, associated with ice and snow (confirmed by plotting subsample mean ice and snow profiles, not shown), becomes stronger and shifts upward with increasing subsample $w_{\rm MAX}$.[9] The general tendency

[8] The Eq. (5) "pressure-buoyancy term" is also weakly positive in the MBL, averaging around 8 m s^{-1} h^{-1} (not shown).

[9] The $w_{\rm MAX}$-Extreme $\overline{q_{\rm FRZ}'}^{S}(k)$ peaks at ~2.1 g kg^{-1} near z = 15.5 km (not shown).

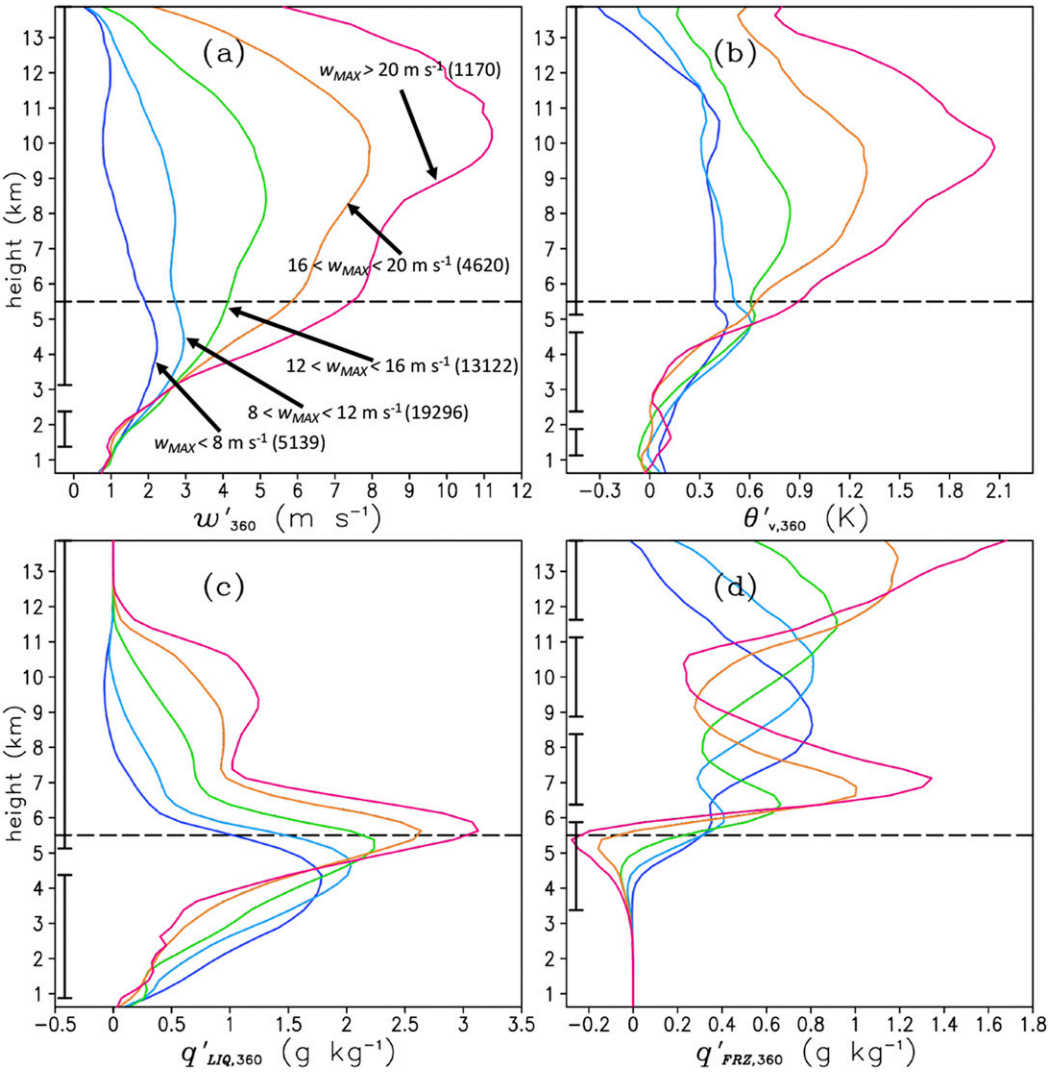

FIG. 11. Vertical profiles of the mean (a) perturbation vertical velocity w'_{360} (m s^{-1}), (b) perturbation virtual potential temperature $\theta'_{v,360}$ (K), (c) perturbation liquid hydrometeor mixing ratio $q'_{\mathrm{LIQ},360}$ (g kg^{-1}), and (d) perturbation frozen hydrometeor mixing ratio $q'_{\mathrm{FRZ},360}$ (g kg^{-1}). Mean values are computed for each subsample of updraft backward trajectories binned by w_{MAX}, as shown by arrows in (a), with the number of trajectories for each subsample given inside parentheses. Bracketed lines enclose vertical layers where the w_{MAX}-12 and w_{MAX}-Extreme subsample mean differences are statistically significant at the 95% level. Dashed horizontal lines denote the approximate melting level height. Perturbation variables are computed with respect to the azimuthal mean.

for the w_{MAX}-Extreme trajectories to loft larger quantities of supercooled water, graupel, ice, and snow to greater heights, compared to other trajectories (Figs. 11c,d), is likely both a consequence of their greater midlevel updraft intensity (Fig. 11a) and a source of fusion LHR contributing to their stronger upper-tropospheric buoyancy (to be shown in section 4d).

b. *Boundary layer thermodynamics*

Can a parcel's w_{MAX} be statistically related to its MBL thermodynamic history? Here we consider only the 31 243 MBL-Origin trajectories that remain in the MBL for at least one hour prior to ascent but which are otherwise stratified by w_{MAX} in the same manner (section 2c). Figure 12a shows time series of subsample $\overline{\theta_e(t)}$ during the final hour of parcel transit through the MBL, where the overbar with "t" as the functional argument denotes an average over all subsample trajectories t minutes prior to exiting the MBL. During their final 15 min in the MBL, the w_{MAX}-Extreme parcels have higher $\overline{\theta_e(t)}$ compared to all other subsamples and their $\overline{\theta_e(t)}$ difference from w_{MAX}-12 is

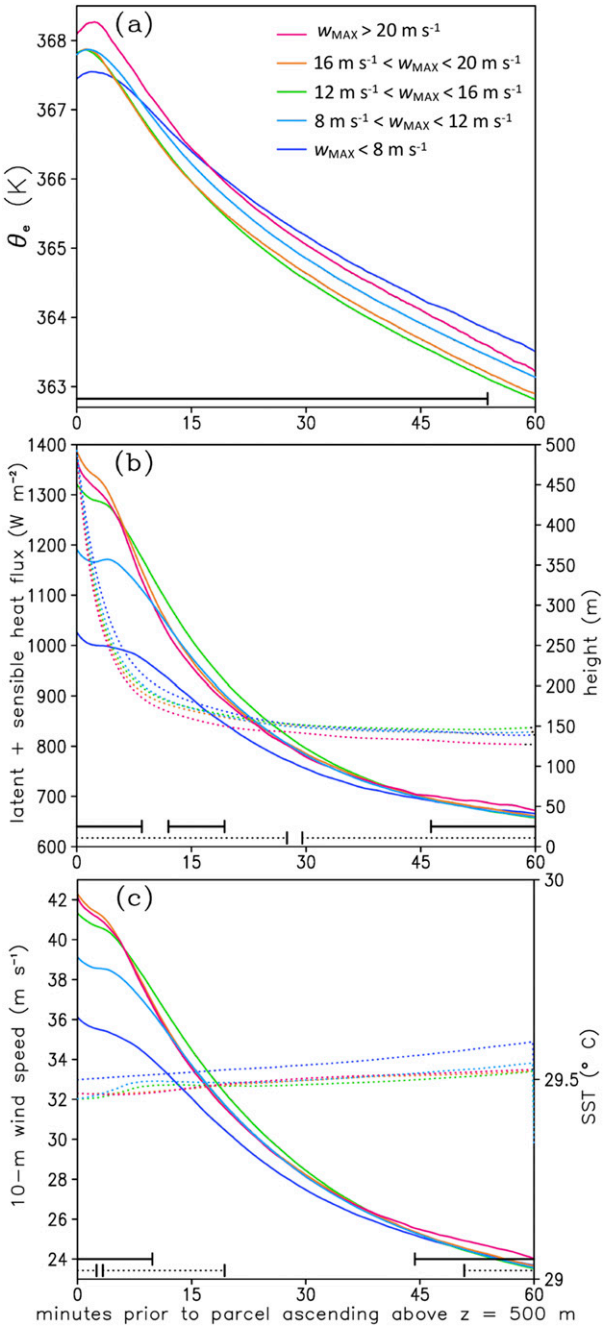

FIG. 12. (a) Mean θ_e (K) for subsamples of backward trajectories binned by w_{MAX}, plotted as a function of time prior to their ascent above $z = 0.5$ km. (b) As in (a), but for mean total (latent + sensible) ocean surface heat flux (W m^{-2}; solid) and parcel height (m; dotted). (c) As in (a), but for 10-m wind speed (m s^{-1}; solid) and SST (°C; dotted). Solid (dot)-bracketed lines denote time intervals where the difference between the w_{MAX}-12 and w_{MAX}-Extreme sample mean θ_e, total surface heat flux, and 10-m wind speed (parcel height and SST) are statistically significant at the 95% level.

statistically significant. Therefore, Wilma's most extreme eyewall updrafts do, on average, originate from pockets of locally higher potential instability in the inner-core MBL.

Given that a near-surface parcel's $D\theta_e/Dt$ is forced in part by surface heat and moisture fluxes (Liu et al. 1999), can differences in MBL $\overline{\theta_e(t)}$ among the w_{MAX}-binned subsamples be attributed to differences in the surface fluxes integrated along surface projections of trajectory paths? Our Wilma (2005) WRF prediction uses the fifth-generation Pennsylvania State University–National Center for Atmospheric Research Mesoscale Model surface layer physics scheme (Grell et al. 1994; Jiménez et al. 2012) to parameterize ocean surface fluxes of sensible heat (H_S) and latent heat (H_L), using the bulk aerodynamic formulas

$$H_S = \rho_a c_p C_H U(\theta_{SST} - \theta_a), \tag{7}$$

and

$$H_L = \rho_a L_v C_Q U(Q_s - Q_a), \tag{8}$$

where c_p is the specific heat capacity at constant pressure; L_v is latent heat of vaporization; θ_{SST} is SST converted to potential temperature; Q_s is the saturated specific humidity at the SST and sea level pressure; ρ_a, θ_a, and Q_a are density, potential temperature, and specific humidity at the bottom model level, respectively; U is the wind speed at the bottom model level added to a parameterized convective wind speed; and the respective heat and moisture bulk transfer coefficients C_H and C_Q are estimated from the surface layer thickness, roughness length, and stability regime using Monin–Obukhov similarity theory (Monin and Obukhov 1954; Zhang and Anthes 1982). The YSU boundary layer scheme (Hong et al. 2006) parameterizes vertical subgrid-scale turbulent mixing of heat and moisture everywhere above the surface layer. The time-invariant SSTs used for this prediction show little variation across Wilma's inner core region (<0.5 K, not shown). Therefore, it is not surprising that Wilma's total surface heat flux ($H = H_S + H_L$) is strongly correlated with 10-m wind speed, as shown in Fig. 13. At RI onset, H is maximized in the northern eyewall, where surface winds are strongest (Fig. 13a). Two hours later, maximum H has become symmetrically distributed throughout the eyewall, consistent with the axisymmetrization of Wilma's surface wind field (Fig. 13c).

The w_{MAX}-Extreme trajectories overlay statistically significant higher $\overline{H(t)}$ compared to w_{MAX}-12 during their final 8 min in the MBL (Fig. 12b); time series of $\overline{H_s(t)}$ and $\overline{H_L(t)}$ show similar variation among subsamples (not shown). Also, note that w_{MAX}-Extreme trajectories

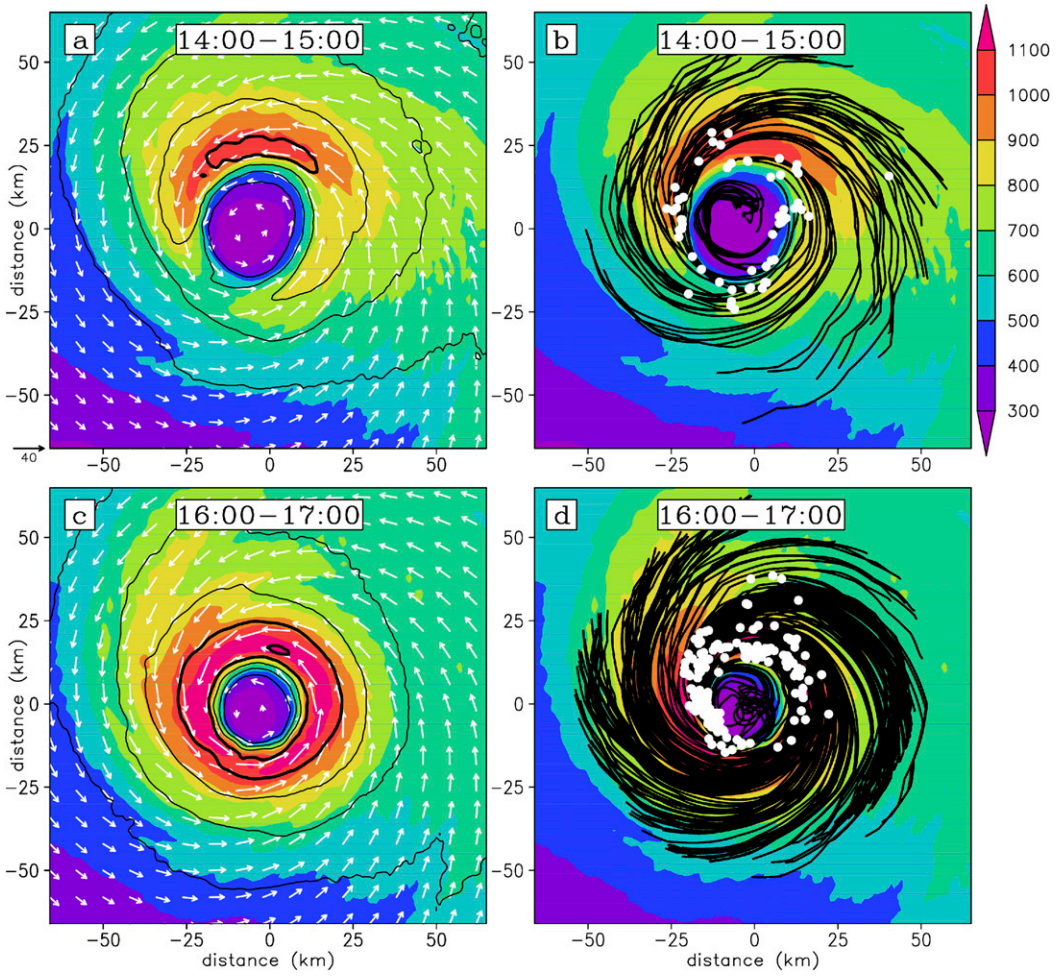

FIG. 13. (a) WRF-predicted total (latent + sensible) ocean surface heat flux (shaded; W m^{-2}), 10-m horizontal wind speed (thin contours for 20, 25, and 30 m s^{-1}; thick contours for 35 and 40 m s^{-1}), and 10-m flow vectors (m s^{-1}), with all variables averaged over the 1-h period ending at 15:00. (b) As in (a), but showing the x–y planar projections (black lines) of all w_{MAX}-20 and w_{MAX}-Extreme trajectories that ascend above z = 0.5 km over the ±5 min period centered on 15:00. Trajectories plotted here show only the final 1-h period of MBL transit, and white dots denote positions where each parcel ascends out of the MBL. (c),(d) As in (a) and (b), but for WRF fields averaged over the 1-h period ending at 17:00 in (c) and w_{MAX}-20 and w_{MAX}-Extreme trajectories ascending above z = 0.5 km over the ±5 min interval surrounding 17:00 in (d).

tend to originate from lower layers in the MBL (i.e., closer to the oceanic heat and moisture source), compared to other trajectories (Fig. 12b). Interestingly, differences among the subsamples in 10-m wind speed along trajectory horizontal projections, $\overline{\text{wspd10}(t)}$, closely mirror those in $\overline{H(t)}$ (Figs. 12b,c). Our finding that the stronger updraft subsamples (i.e., w_{MAX}-Extreme, w_{MAX}-20, and w_{MAX}-16) have higher $\overline{\text{wspd10}(t)}$ and $\overline{H(t)}$ compared to w_{MAX}-12 trajectories during their final 8 min in the MBL implies that TC updraft intensity depends to some extent on *wind-induced* surface heat fluxes and not only on preexisting conditional instability. When considering these stronger updrafts' contribution to the azimuthally averaged eyewall updraft core intensity, these results support Emanuel (1986)'s WISHE model. We should use caution, however, when generalizing these results to other TCs, given their potential sensitivity to the WRF boundary layer and surface layer physics parameterizations and to the time-invariant, relatively horizontally homogenous SST field.

Finally, note that $\overline{H}(t)$ and $\overline{\text{wspd10}(t)}$ remain relatively tightly clustered among w_{MAX}-Extreme, w_{MAX}-20, and w_{MAX}-16 trajectories (Figs. 12b,c), even though w_{MAX}-Extreme parcels are distinguished from the others by their higher θ_e upon departing the MBL (Fig. 12a). This could potentially reflect the fact that some of Wilma's strongest updrafts originate from the eye MBL (Figs. 13b,d), where H is small due to the calm

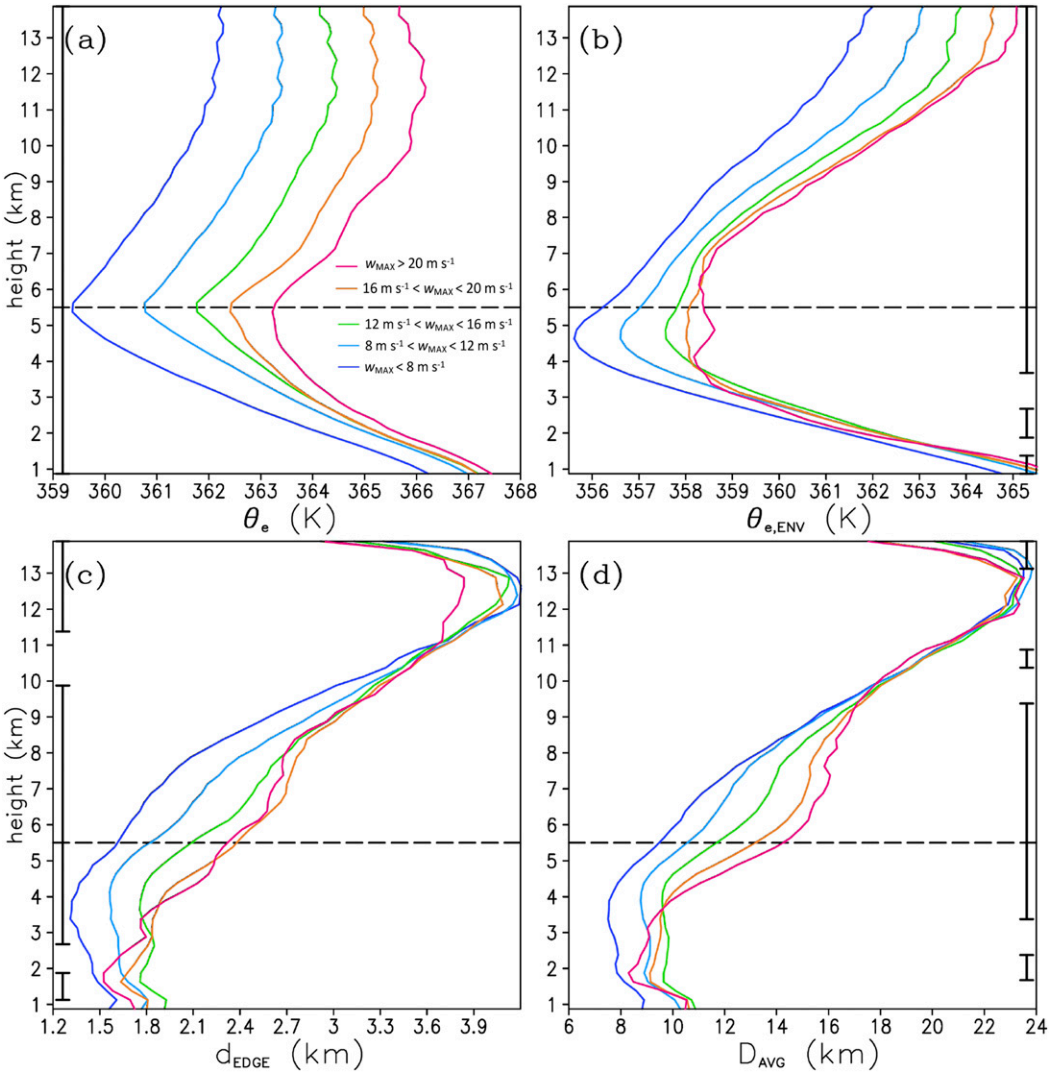

FIG. 14. (a) As in Fig. 11, but for the subsample mean θ_e(K) (b) As in (a), but for subsample mean environmental θ_e ($\theta_{e,ENV}$; K). (c) As in (a), but for the subsample mean smallest distance in any cardinal direction to the updraft element boundary d_{EDGE} (km). (d) As in (a), but for the subsample mean updraft element diameter D_{AVG} (km). See section 2e for details on the computation of $\theta_{e,ENV}$.

winds but where MBL θ_e is locally the highest (Fig. 6a), likely due to eye parcels' relatively long residence time. Previous TC simulation studies have also identified the eye MBL as a source region for high-θ_e parcels that later become stirred into eyewall updrafts (Liu et al. 1999; Braun 2002; Persing and Montgomery 2003; Cram et al. 2007; Hazelton et al. 2017); Guimond et al. (2016) showed observational evidence of this process.

c. *Environmental air entrainment*

Figure 14a compares mean θ_e profiles among the five subsamples. Here we assume that below the melting level, where fusion LHR can be neglected, the magnitude of a parcel's θ_e decrease as it rises above the MBL can be treated as a rough proxy for cumulative environmental air entrainment. It is worth reminding the reader that this study treats updraft elements as aggregations of adjacent parcels that are distinguished from the surrounding environment by their having $w > 0.5$ m s^{-1} and RH > 95% (section 2e). At $z = 1$ km, w_{MAX}-Extreme trajectories have statistically significant larger $\overline{\theta_e}^S(k)$ compared to w_{MAX}-12 trajectories. Between the MBL and the melting level, $\overline{\theta_e}^S(k)$ decreases with height for all subsamples; however, θ_e nonconservation becomes more pronounced as w_{MAX} decreases. Therefore, Wilma's strongest updraft parcels, on average, are likely distinguished from the background secondary circulation in part by their lower entrainment rates. Above the melting level,

$\overline{\theta_e}^S(k)$ increases with height at a similar rate for all subsamples, perhaps due to a combination of fusion LHR (Fierro et al. 2009, 2012; M15) and mixing with an environment where θ_e also increases with height (cf. Figs. 14a,b).

Figures 14c and 14d show that w_{MAX}-Extreme trajectories have statistically significant larger $\overline{d_{EDGE}}^S(k)$ and $\overline{D_{AVG}}^S(k)$, respectively, over the z = 3–9-km layer as compared to w_{MAX}-12 trajectories. Examining how a histogram of w_{MAX}-Extreme and w_{MAX}-12 trajectories binned by d_{EDGE} varies with height in Fig. 15a, we find that the low-level distribution peaks at $d_{EDGE} < 2$ km for both subsamples. However, the z = 4.5–8-km layer histogram peak shifts to d_{EDGE} = 2–3 km for w_{MAX}-Extreme while remaining at d_{EDGE} = 1–2 km for w_{MAX}-12. Binning w_{MAX}-Extreme and w_{MAX}-12 trajectories by D_{AVG} yields similar patterns (Fig. 15b). These findings agree with Morrison (2017), who used idealized WRF simulations to show that narrower (wider) updrafts experience more (less) dilution, leading to greater (less) reduction in buoyancy. However, it is also quite plausible that the differences among subsamples in $\overline{\theta_e}^S(k)$ and $\overline{d_{EDGE}}^S(k)$ shown in Figs. 14a and 14c could simply reflect the fact that a significant fraction of the weaker updraft trajectories (i.e., those belonging to w_{MAX}-8 and w_{MAX}-12) are located on the edges of stronger updraft cores. Perhaps most significantly, these results suggest that environmental air entrainment can strongly modulate TC eyewall updraft intensity, even for cases such as Wilma (2005) that develop in environments with relatively high RH in the low-to-middle troposphere (see Fig. 2 in CZ11).

d. Statistical vertical momentum budget

Finally, let us extend the section 3c vertical momentum budget analysis to a larger trajectory sample. Figure 16a shows that $\overline{BA}^S(k)$ increases with subsample w_{MAX} over the z = 2–9-km layer. Between z = 1.5 km and the melting level, w_{MAX}-12 (w_{MAX}-8) have very small (negative) $\overline{BA}^S(k)$ and positive $\overline{PGA}^S(k)$. Above the melting level, all subsamples have positive $\overline{BA}^S(k)$ and negative $\overline{PGA}^S(k)$ (Fig. 16a), consistent with idealized updraft simulations with minimal dynamic contributions to the p' field (Markowski and Richardson 2010; Morrison 2016). Interestingly, all subsamples have a similar $\overline{PGA}^S(k)$ magnitude between the melting level and z = 10.5 km. As a result, $\overline{BA}^S(k)$ and $\overline{PGA}^S(k)$ nearly cancel for w_{MAX}-8 and w_{MAX}-12, consistent with their near zero $\overline{Dw/Dt}^S(k)$, while $|\overline{BA}^S(k)| > |\overline{PGA}^S(k)|$ for the stronger updraft groups, consistent with their positive $\overline{Dw/Dt}^S(k)$ (cf. Figs. 16a,b). For individual trajectories, BA(k) and PGA(k) are generally anticorrelated in a deep layer (Figs. 17a,b), and a scatterplot of z = 10-km BA versus PGA further shows that BA + PGA > 0 for most w_{MAX}-Extreme trajectories but for only ~50% of w_{MAX}-12 trajectories (Fig. 17b).

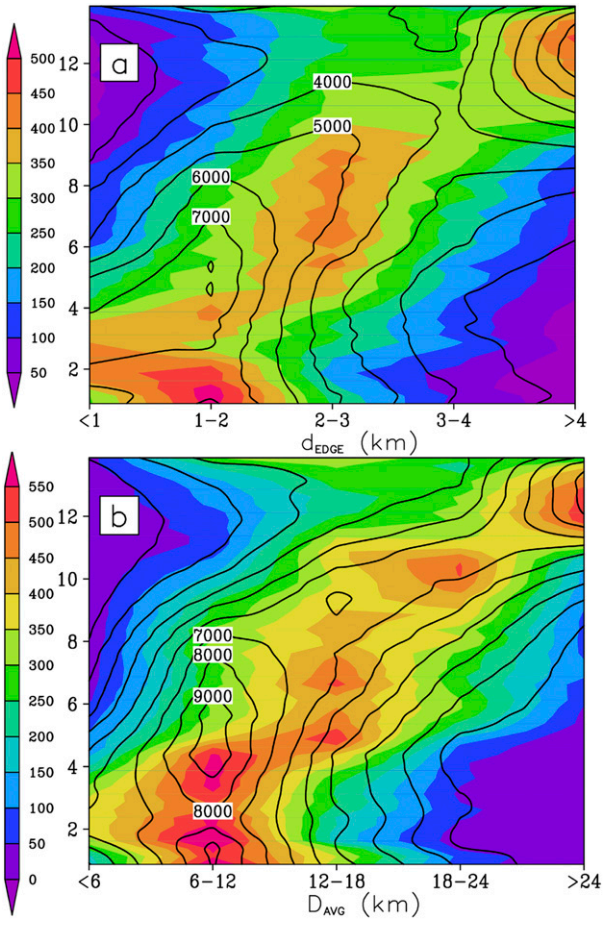

FIG. 15. (a) Histogram showing the number of updraft trajectories from the w_{MAX}-Extreme subsample (shaded), binned by distance to the updraft edge (km), as shown on the x axis, as a function of height (km), as shown on the y axis. Black contours show the number of updraft trajectories from the w_{MAX}-12 subsample, binned in the same manner. (b) As in (a), but for w_{MAX}-Extreme and w_{MAX}-12 trajectories binned by updraft diameter.

How do the relative contributions of thermal buoyancy and hydrometeor loading to the BA change with increasing w_{MAX}? Figure 16c shows that subsample $\overline{g(\theta_v'/\overline{\theta_v})}^S(k)$ becomes more largely positive with increasing w_{MAX} between the melting level and z = 14 km. Above z = 1.5 km, w_{MAX}-Extreme trajectories are distinguished from all others by their larger positive $\overline{g(\theta_v'/\overline{\theta_v})}^S(k)$, consistent with the fact that w_{MAX}-Extreme trajectories are also distinguished from all others by their higher $\overline{\theta_e}(t)$ upon exiting the MBL (cf. Figs. 12a and 16c). Another interesting w_{MAX}-Extreme trajectory characteristic is their statistically significant smaller $\overline{gq_{HYD}'}^S(k)$ magnitude relative to w_{MAX}-12 trajectories over the z = 3–5-km layer (Fig. 16d). Furthermore, among w_{MAX}-12, w_{MAX}-16, and

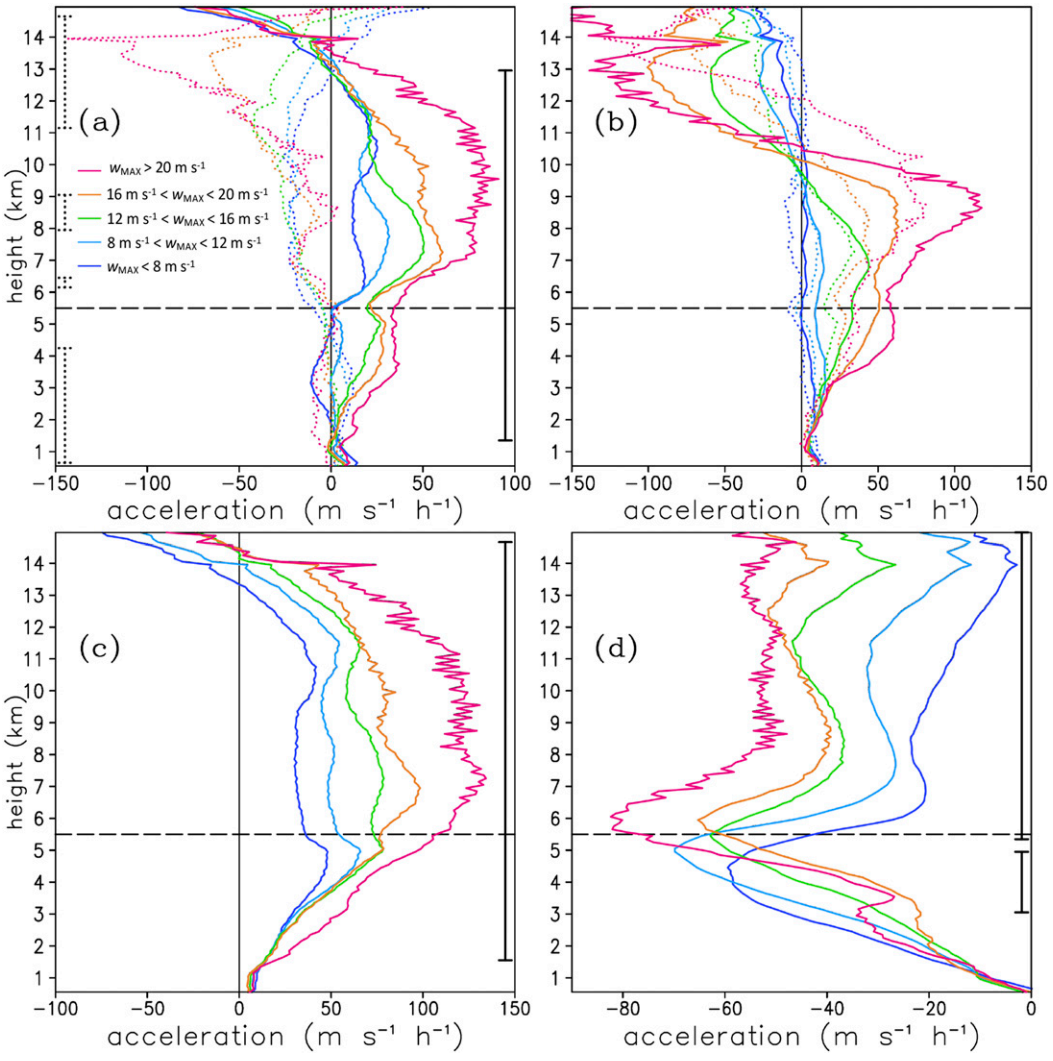

FIG. 16. (a) Vertical profiles of trajectory subsample mean BA (solid lines; m s^{-1} h^{-1}) and PGA (dotted lines; m s^{-1} h^{-1}), color coded by subsample w_{MAX} range as in Fig. 11. (b) As in (a), but for subsample mean parcel vertical acceleration Dw/Dt (solid lines; m s^{-1} h^{-1}) and sum of the subsample mean BA and PGA (dotted lines; m s^{-1} h^{-1}). (c) As in (a), but for subsample mean thermal buoyancy $g\theta_v'/\overline{\theta_v}$ (solid lines; m s^{-1} h^{-1}). (d) As in (b), but for subsample mean hydrometeor loading gq_{HYD}' (solid lines; m s^{-1} h^{-1}). The dashed black line denotes the approximate melting level. Bracketed solid lines lines in (a),(c),(d) show height intervals over which differences in the w_{MAX}-12 and w_{MAX}-Extreme mean BA, $g\theta_v'/\overline{\theta_v}$, and gq_{HYD}', respectively, are statistically significant at the 95% level; bracketed dotted lines in (a) show the same for differences in PGA.

w_{MAX}-20 in this same layer, hydrometeor loading weakens with increasing w_{MAX} (Fig. 16d). This could result from both (i) delayed warm-rain processes in stronger mid-level updrafts (Fig. 11a) as cloud droplets are more rapidly carried upward, similar to bounded weak echo regions in supercells; and (ii) v_t advecting the bulk of hydrometeor fallout cyclonically downwind of the stronger, better-organized low-to-middle tropospheric updraft cores, as suggested by Fig. 10b. Further research investigating the impacts of hydrometeor loading on TC eyewall updrafts and their sensitivity to model microphysics could be beneficial. For all subsamples, $g(\theta_v'/\overline{\theta_v})(k)$ and $gq_{HYD}'(k)$ are strongly anticorrelated in the middle and upper troposphere, which might be expected, given that stronger updrafts can loft more hydrometeors (Fig. 17c). Nevertheless, positive $g(\theta_v'/\overline{\theta_v})(k)$ outweighs negative $gq_{HYD}'(k)$ for most w_{MAX}-Extreme trajectories at $z = 8$ km (Fig. 17d).

5. Summary and conclusions

This study investigates the three-dimensional structure and thermodynamics of Hurricane Wilma's (2005)

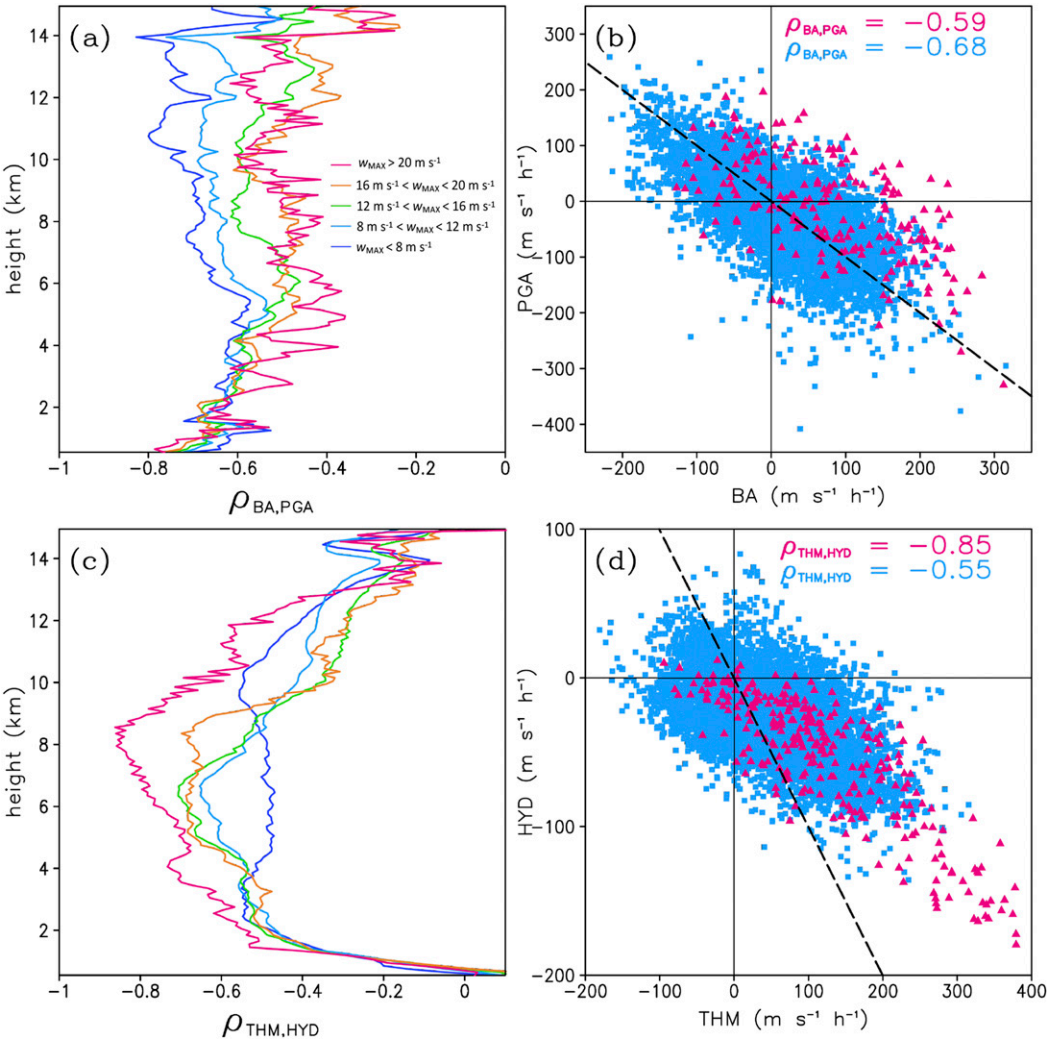

FIG. 17. (a) Pearson correlation coefficient between the BA and PGA ($\rho_{BA,PGA}$) plotted for each w_{MAX}-binned subsample as a function of height, with lines colored by subsample w_{MAX} range as in Figs. 11 and 16. (b) Scatterplot of BA and PGA at z = 10 km for w_{MAX}-12 (light blue dots) and w_{MAX}-Extreme (magenta triangles). (c) As in (a), but for the correlation coefficient between thermal buoyancy (THM) and hydrometeor loading (HYD) ($\rho_{THM,HYD}$). (d) As in (b), but for the z = 8-km scatterplot of THM and HYD. Trajectories to the right of the dashed line in (b) have BA + PGA > 0, and trajectories to the right of the dashed line in (d) have THM + HYD > 0.

eyewall updrafts from a Lagrangian perspective. For this purpose, we ran 97 020 four-hour backward trajectories using winds output from a Hurricane Wilma (2005) WRF prediction. All trajectories are seeded from Wilma's upper-tropospheric eyewall over a 4-h period beginning just after RI onset. Of the 97 020 backward trajectories, the ~45% originating in the MBL are binned by w_{MAX} and saved for analysis in this study.

First, we compared a trajectory run through an intense CB core, with ~30 m s^{-1} w_{MAX}, against a background secondary circulation trajectory in terms of their three-dimensional structure, θ_e tendencies, and vertical momentum budgets. Key findings are as follows:

- The CB core parcel ascends from the MBL to z = 14 km in ~31 min, completing one-half circle around the eyewall. In contrast, the secondary circulation parcel ascends the same vertical distance over ~83 min, completing 1.5 circles around the eyewall.
- Both the CB core and secondary circulation parcels exit the MBL with high θ_e–366 and 368 K, respectively. Although both parcels experience θ_e reduction while ascending to the melting level followed by θ_e recovery in the upper troposphere, the low-to-middle tropospheric θ_e decline is significantly smaller for the CB core parcel (~−3 K) compared to the secondary circulation parcel (~−8 K).

- A weakly positive BA lifts the CB core parcel out of the MBL. This positive BA becomes stronger with height through the upper troposphere, on account of positive thermal buoyancy more than offsetting hydrometeor loading – the former peaking at ~330 m s^{-1} h^{-1} near z = 8 km. As a result, w increases nearly monotonically with height toward a $z \sim 13$ km w_{MAX}. A large negative PGA rapidly decelerates w at higher levels.
- The secondary circulation parcel originates in a heavy-precipitating portion of the MBL, and a positive PGA helps lift it into the free troposphere. Unlike for the CB core parcel, thermal buoyancy remains mostly positive but much weaker throughout ascent, generally <50 m s^{-1} h^{-1}. Increasing hydrometeor loading, together with a negative PGA, offsets the weak positive thermal buoyancy as the parcel approaches the melting level, resulting in deceleration to near zero w. Rapid hydrometeor unloading above the melting level helps accelerate this parcel vertically toward its upper-level w_{MAX}.

Next, we stratified a large batch of eyewall updraft trajectories by w_{MAX} into five subsamples and compared subsample mean profiles of θ_e, vertical acceleration terms, as well as other variables expected to impact the BA and θ_e conservation under saturated conditions. Parcels achieving the most extreme updraft speeds exceeding 20 m s^{-1} were most strongly distinguished from those more representative of the background secondary circulation (i.e., parcels with 8 m s^{-1} $\leq$ w_{MAX} $\leq$ 12 m s^{-1}) by their (i) trajectory paths overlaying higher ocean surface latent and sensible heat fluxes during their last 8 min transiting the MBL; (ii) higher θ_e during their last 15 min transiting the MBL; (iii) greater θ_e conservation (i.e., less θ_e reduction in the low-to-middle troposphere); (iv) being embedded deeper inside of updraft elements; (v) belonging to wider updraft elements; (vi) reduced hydrometeor loading over the z = 3–5-km layer; (vii) larger thermal buoyancy above z = 1.5 km; and (viii) higher supercooled liquid water and frozen hydrometeor mixing ratios above the melting level.

The above results suggest that Wilma's strongest eyewall updrafts are rooted in portions of the MBL with locally enhanced θ_e and ocean surface heat/moisture fluxes. They support CZ13, who found that reducing SSTs[10] by 1°C significantly reduces Wilma's CB activity, upper level warming, and RI rate. They also support some aspects of Emanuel (1986, 1997)'s WISHE hypothesis—namely, that wind-induced ocean surface heat and moisture fluxes provide the thermodynamic heat source driving TC intensification. However, in identifying localized stronger updrafts that are positively buoyant relative to the eyewall background state, this study supports other recent work (Heymsfield et al. 2001; Braun 2002; Eastin et al. 2005a,b) in disagreement with WISHE's assumption that eyewall ascent is slantwise moist neutral everywhere. CZ13 and M15 also showed how CB updraft compensating subsidence may have contributed to Wilma's upper level warm core development and resulting P_{MIN} intensification.

This study also identifies two midlevel processes that may have helped differentiate Wilma's most intense eyewall updraft parcels from background secondary circulation parcels leaving the MBL with similarly high θ_e: environmental air entrainment and hydrometeor loading. Compared to the w_{MAX}-12 subsample, the w_{MAX}-Extreme parcels' smaller θ_e reduction while ascending below the melting level is consistent with their larger thermal buoyancy, suggesting that the w_{MAX}-Extreme parcels experience reduced mixing with the lower-θ_e environmental air, given that θ_e is conserved under inviscid pseudoadiabatic ascent. This is consistent with w_{MAX}-Extreme trajectories being distinguished from the other trajectories in terms of their wider surrounding updraft elements, on average. Second, hydrometeor loading generally weakens with increasing w_{MAX} over the z = 3–5-km layer. Wilma's strongest eyewall updrafts become most thermodynamically distinct from the background secondary circulation, in terms of their enhanced thermal buoyancy and w, in the upper troposphere. The above results are supported by Zipser (2003) who showed, using parcel theory and a representative tropical oceanic environmental sounding, how a relatively small decrease in midlevel updraft dilution could increase midtropospheric w by ~5 m s^{-1} and loft considerably more condensate above the melting level, resulting in a significant boost to upper-tropospheric updraft intensity through enhanced fusion LHR.

To some extent, our findings bridge those of CZ13 and M15, who focused separately on the importance of high SSTs and upper-tropospheric fusion LHR to the development of Wilma's CBs. Both w_{MAX}-20 and w_{MAX}-Extreme trajectories transited through cores of CB updraft elements. However, one limitation of the methods used here is that they could not readily describe systematic differences in the *updraft element* characteristics surrounding the different w_{MAX}-binned trajectory

[10] As shown in Eqs. (7) and (8), heat and moisture fluxes directed from the ocean to the atmosphere are proportional to the air-sea thermodynamic disequilbrium, which depends not only on SST but also on the temperature, pressure, and moisture content of the atmospheric surface layer.

subsamples. For example, what fraction of w_{MAX}-12 trajectories ascended along the outer edges of CB elements, and what fraction completed their full ascent within weaker updraft elements? A follow-up study that combines trajectory analysis with object-based methods designed to track large samples of updraft elements over time could shed further light on physical processes favorable to CB development in TCs. The sensitivity of these results to the choice of microphysics parameterization scheme should also be explored.

As for any case study, future work is needed in order to determine how generally these results apply to eyewall updrafts in other TCs. Hurricane Wilma (2005) may be considered a ''prototype case'' for TCs undergoing extreme RI under near-ideal environmental conditions. It may be particularly worthwhile to investigate how VWS affects CB structure and thermodynamics. Further research could more deeply explore dynamical features identified in previous studies that may facilitate CB initiation by enhancing low-level convergence; these include eyewall mesovortices arising from barotropic instability (Braun et al. 2006; Guimond et al. 2016; Hazelton et al. 2017) and VWS-induced wavenumber-1 asymmetries in the MBL inflow intensity (Reasor et al. 2013; Rogers et al. 2015; Hazelton et al. 2017). Trajectory analysis could also be useful for studying CB contributions to the total upward mass flux in a TC eyewall and the outflow expansion. Given the important role that CBs appear to play in TC intensification, it is necessary to develop a more complete understanding of the inner-core processes favoring their development.

Acknowledgments. This work was funded by the U.S. Office of Naval Research Grants N000141410143 and N000141712210. The authors acknowledge the University of Maryland supercomputing resources (http://hpcc.umd.edu) made available for conducting the research reported in this paper. The authors also wish to give special thanks to Dr. Xin Liu, Chinese Academy of Meteorological Sciences, for developing the Matlab scripts used for plotting the trajectory output in three dimensions.

Data availability statement. The authors have archived the Hurricane Wilma (2005) WRF prediction, all trajectory output data used in this study, as well as source codes for computing trajectory positions and the diagnostic variables listed in Tables 1–3 on the University of Maryland College Park Atmospheric and Oceanic Sciences departmental Linux server. These files can be made available to anyone upon request.

REFERENCES

Black, M. L., R. W. Burpee, and F. D. Marks Jr., 1996: Vertical motion characteristics of tropical cyclones determined with airborne Doppler radial profiles. *J. Atmos. Sci.*, **53**, 1887–1909, https://doi.org/10.1175/1520-0469(1996)053<1887:VMCOTC>2.0.CO;2.

Bolton, D., 1980: The computation of equivalent potential temperature. *Mon. Wea. Rev.*, **108**, 1046–1053, https://doi.org/10.1175/1520-0493(1980)108<1046:TCOEPT>2.0.CO;2.

Braun, S. A., 2002: A cloud-resolving simulation of Hurricane Bob (1991): Storm structure and eyewall buoyancy. *Mon. Wea. Rev.*, **130**, 1573–1592, https://doi.org/10.1175/1520-0493(2002)130<1573:ACRSOH>2.0.CO;2.

——, M. T. Montgomery, and X. Pu, 2006: High-resolution simulation of Hurricane Bonnie (1998). Part I: The organization of eyewall vertical motion. *J. Atmos. Sci.*, **63**, 19–42, https://doi.org/10.1175/JAS3598.1.

Charney, J. G., and A. Eliassen, 1964: On the growth of the hurricane depression. *J. Atmos. Sci.*, **21**, 68–75, https://doi.org/10.1175/1520-0469(1964)021<0068:OTGOTH>2.0.CO;2.

Chen, H., and D.-L. Zhang, 2013: On the rapid intensification of Hurricane Wilma (2005). Part II: Convective bursts and the upper-level warm core. *J. Atmos. Sci.*, **70**, 146–162, https://doi.org/10.1175/JAS-D-12-062.1.

——, and S. G. Gopalakrishnan, 2015: A study on the asymmetric rapid intensification of Hurricane Earl (2010) using the HWRF system. *J. Atmos. Sci.*, **72**, 531–550, https://doi.org/10.1175/JAS-D-14-0097.1.

——, D.-L. Zhang, J. Carton, and R. Atlas, 2011: On the rapid intensification of Hurricane Wilma (2005). Part I: Model prediction and structural changes. *Wea. Forecasting*, **26**, 885–901, https://doi.org/10.1175/WAF-D-11-00001.1.

Cram, T. A., J. Persing, M. T. Montgomery, and S. A. Braun, 2007: A Lagrangian trajectory view on transport and mixing processes between the eye, eyewall, and environment using a high-resolution simulation of Hurricane Bonnie (1998). *J. Atmos. Sci.*, **64**, 1835–1856, https://doi.org/10.1175/JAS3921.1.

Eastin, M. D., W. M. Gray, and P. G. Black, 2005a: Buoyancy of convective vertical motions in the inner core of intense hurricanes. Part I: General statistics. *Mon. Wea. Rev.*, **133**, 188–208, https://doi.org/10.1175/MWR-2848.1.

——, ——, and ——, 2005b: Buoyancy of convective vertical motions in the inner core of intense hurricanes. Part II: Case studies. *Mon. Wea. Rev.*, **133**, 209–227, https://doi.org/10.1175/MWR-2849.1.

Emanuel, K. A., 1986: An air–sea interaction theory for tropical cyclones. Part I: Steady-state maintenance. *J. Atmos. Sci.*, **43**, 585–605, https://doi.org/10.1175/1520-0469(1986)043<0585:AASITF>2.0.CO;2.

——, 1997: Some aspects of hurricane inner-core dynamics and energetics. *J. Atmos. Sci.*, **54**, 1014–1026, https://doi.org/10.1175/1520-0469(1997)054<1014:SAOHIC>2.0.CO;2.

Fierro, A. O., J. Simpson, M. A. LeMone, J. M. Straka, and B. F. Smull, 2009: On how hot towers fuel the Hadley cell: An observational and modeling study of line-organized convection in the equatorial trough from TOGA COARE. *J. Atmos. Sci.*, **66**, 2730–2746, https://doi.org/10.1175/2009JAS3017.1.

——, E. J. Zipser, M. A. LeMone, J. M. Straka, and J. Simpson, 2012: Tropical oceanic hot towers: Need they be undilute to transport energy from the boundary layer to the upper troposphere effectively? An answer based on trajectory analysis

of a simulated TOGA-COARE convective system. *J. Atmos. Sci.*, **69**, 195–213, https://doi.org/10.1175/JAS-D-11-0147.1.

Fritsch, J. M., and R. A. Maddox, 1981: Convectively driven mesoscale weather systems aloft. Part I: Observations. *J. Appl. Meteor.*, **20**, 9–19, https://doi.org/10.1175/1520-0450(1981)020<0009:CDMWSA>2.0.CO;2.

Gal-Chen, T., 1982: Errors in fixed and moving frame of references: Applications for conventional and Doppler radar analysis. *J. Atmos. Sci.*, **39**, 2279–2300, https://doi.org/10.1175/1520-0469(1982)039<2279:EIFAMF>2.0.CO;2.

Gentry, R. C., T. T. Fujita, and R. C. Sheets, 1970: Aircraft, spacecraft, satellite, and radar observations of Hurricane Gladys, (1968). *J. Appl. Meteor.*, **9**, 837–850, https://doi.org/10.1175/1520-0450(1970)009<0837:ASSARO>2.0.CO;2.

Grell, G. A., J. Dudhia, and D. R. Stauffer, 1994: A description of the fifth-generation Penn State/NCAR Mesoscale Model (MM5). NCAR Tech. Note NCAR/TN-398+STR, 121 pp., https://doi.org/10.5065/D60Z716B.

Guimond, S. R., G. H. Heymsfield, and F. J. Turk, 2010: Multiscale observations of Hurricane Dennis (2005): The effects of hot towers on rapid intensification. *J. Atmos. Sci.*, **67**, 633–654, https://doi.org/10.1175/2009JAS3119.1.

——, ——, P. D. Reasor, and A. C. Didlake, 2016: The rapid intensification of Hurricane Karl (2010): New remote sensing observations of convective bursts from a Global Hawk platform. *J. Atmos. Sci.*, **73**, 3617–3639, https://doi.org/10.1175/JAS-D-16-0026.1.

Hack, J. J., and W. H. Schubert, 1986: Nonlinear response of atmospheric vortices to heating by organized cumulus convection. *J. Atmos. Sci.*, **43**, 1559–1573, https://doi.org/10.1175/1520-0469(1986)043<1559:NROAVT>2.0.CO;2.

Hazelton, A. T., R. F. Rogers, and R. E. Hart, 2017: Analyzing simulated convective bursts in two Atlantic Hurricanes. Part I: Burst formation and development. *Mon. Wea. Rev.*, **145**, 3073–3094, https://doi.org/10.1175/MWR-D-16-0267.1.

Heymsfield, G. M., J. B. Halverson, J. Simpson, L. Tian, and T. P. Bui, 2001: ER-2 Doppler radar investigations of the eyewall of Hurricane Bonnie during the convection and moisture experiment-3. *J. Appl. Meteor.*, **40**, 1310–1330, https://doi.org/10.1175/1520-0450(2001)040<1310:EDRIOT>2.0.CO;2.

Hildebrand, P. H., and Coauthors, 1996: The ELDORA/ASTRAIA airborne Doppler weather radar: High-resolution observations from TOGA COARE. *Bull. Amer. Meteor. Soc.*, **77**, 213–232, https://doi.org/10.1175/1520-0477(1996)077<0213:TEADWR>2.0.CO;2.

Hogsett, W., and D.-L. Zhang, 2009: Numerical simulation of Hurricane Bonnie (1998). Part III: Energetics. *J. Atmos. Sci.*, **66**, 2678–2696, https://doi.org/10.1175/2009JAS3087.1.

Hong, S.-Y., Y. Noh, and J. Dudhia, 2006: A new vertical diffusion package with an explicit treatment of entrainment processes. *Mon. Wea. Rev.*, **134**, 2318–2341, https://doi.org/10.1175/MWR3199.1.

Houze, R. A., Jr., 1993: *Cloud Dynamics*. Academic Press, 573 pp.

——, W.-C. Lee, and M. Bell, 2009: Convective contribution to the genesis of Hurricane Ophelia (2005). *Mon. Wea. Rev.*, **137**, 2778–2800, https://doi.org/10.1175/2009MWR2727.1.

Jiménez, P. A., J. Dudhia, J. F. González-Rouco, J. Navarro, J. P. Montávez, and E. García-Bustamante, 2012: A revised scheme for the WRF surface layer formulation. *Mon. Wea. Rev.*, **140**, 898–918, https://doi.org/10.1175/MWR-D-11-00056.1.

Jorgensen, D. P., 1984: Mesoscale and convective-scale characteristics of mature hurricanes. Part II: Inner core structure of Hurricane Allen (1980). *J. Atmos. Sci.*, **41**, 1287–1311, https://doi.org/10.1175/1520-0469(1984)041<1287:MACSCO>2.0.CO;2.

——, E. J. Zipser, and M. A. LeMone, 1985: Vertical motions in intense hurricanes. *J. Atmos. Sci.*, **42**, 839–856, https://doi.org/10.1175/1520-0469(1985)042<0839:VMIIH>2.0.CO;2.

Kaplan, J., and M. DeMaria, 2003: Large-scale characteristics of rapidly intensifying tropical cyclones in the North Atlantic basin. *Wea. Forecasting*, **18**, 1093–1108, https://doi.org/10.1175/1520-0434(2003)018<1093:LCORIT>2.0.CO;2.

Liu, Y., D.-L. Zhang, and M. K. Yau, 1999: A multiscale numerical study of Hurricane Andrew (1992). Part II: Kinematics and inner-core structures. *Mon. Wea. Rev.*, **127**, 2597–2616, https://doi.org/10.1175/1520-0493(1999)127<2597:AMNSOH>2.0.CO;2.

Markowski, P., and Y. Richardson, 2010: *Mesoscale Meteorology in Midlatitudes*. Wiley-Blackwell, 430 pp.

Marks, F. D., Jr., and R. A. Houze Jr., 1987: Inner core structure of Hurricane Alicia from airborne Doppler radar observations. *J. Atmos. Sci.*, **44**, 1296–1317, https://doi.org/10.1175/1520-0469(1987)044<1296:ICSOHA>2.0.CO;2.

May, P. T., and D. K. Rajopadhyaya, 1996: Wind profiler observations of vertical motion and precipitation microphysics of a tropical squall line. *Mon. Wea. Rev.*, **124**, 621–633, https://doi.org/10.1175/1520-0493(1996)124<0621:WPOOVM>2.0.CO;2.

Miller, W., and D.-L. Zhang, 2019: A three-dimensional trajectory model with advection correction for tropical cyclones: Algorithm description and tests for accuracy. *Mon. Wea. Rev.*, **147**, 3145–3167, https://doi.org/10.1175/MWR-D-18-0434.1.

——, H. Chen, and D.-L. Zhang, 2015: On the rapid intensification of Hurricane Wilma (2005). Part III: Effects of latent heat of fusion. *J. Atmos. Sci.*, **72**, 3829–3849, https://doi.org/10.1175/JAS-D-14-0386.1.

Molinari, J., P. Dodge, D. Vollaro, K. L. Corbosiero, and F. Marks Jr., 2006: Mesoscale aspects of the downshear reformation of a tropical cyclone. *J. Atmos. Sci.*, **63**, 341–354, https://doi.org/10.1175/JAS3591.1.

Monin, A. S., and A. M. Obukhov, 1954: Basic laws of turbulent mixing in the atmosphere near the ground. *Tr. Inst. Teor. Geofiz. Akad. Nauk SSSR*, **24**, 1963–1987.

Montgomery, M. T., and R. K. Smith, 2014: Paradigms for tropical-cyclone intensification. *Aust. Meteor. Oceanogr. J.*, **64**, 37–66, https://doi.org/10.22499/2.6401.005.

——, M. E. Nicholls, T. A. Cram, and A. B. Saunders, 2006: A vortical hot tower route to tropical cyclogenesis. *J. Atmos. Sci.*, **63**, 355–386, https://doi.org/10.1175/JAS3604.1.

Morrison, H., 2016: Impacts of updraft size and dimensionality on the perturbation pressure and vertical velocity in cumulus convection. Part I: Simple, generalized analytic solutions. *J. Atmos. Sci.*, **73**, 1441–1454, https://doi.org/10.1175/JAS-D-15-0040.1.

——, 2017: An analytic description of the structure and evolution of growing deep cumulus updrafts. *J. Atmos. Sci.*, **74**, 809–834, https://doi.org/10.1175/JAS-D-16-0234.1.

Morton, B. R., G. Taylor, and J. S. Turner, 1956: Turbulent gravitational convection from maintained and instantaneous sources. *Proc. Roy. Soc. London*, **234A**, 1–23, https://doi.org/10.1098/rspa.1956.0011.

Nguyen, L. T., and J. Molinari, 2015: Simulation of the downshear reformation of a tropical cyclone. *J. Atmos. Sci.*, **72**, 4529–4551, https://doi.org/10.1175/JAS-D-15-0036.1.

Nguyen, S. V., R. K. Smith, and M. T. Montgomery, 2008: Tropical-cyclone intensification and predictability in three dimensions. *Quart. J. Roy. Meteor. Soc.*, **134**, 563–582, https://doi.org/10.1002/qj.235.

Nolan, D. S., 2007: What is the trigger for tropical cyclogenesis? *Aust. Meteor. Mag.*, **56**, 241–266.

Ooyama, K., 1969: Numerical simulation of the lifecycle of tropical cyclones. *J. Atmos. Sci.*, **26**, 3–40, https://doi.org/10.1175/1520-0469(1969)026<0003:NSOTLC>2.0.CO;2.

——, 1982: Conceptual evolution of the theory and modeling of the tropical cyclone. *J. Meteor. Soc. Japan*, **60**, 369–380, https://doi.org/10.2151/jmsj1965.60.1_369.

Pasch, R. J., E. S. Blake, H. D. Cobb III, and D. P. Roberts, 2006: Tropical cyclone report: Hurricane Wilma (15–25 October 2005). NOAA/NHC Tech. Rep. AL252005, 27 pp., https://www.nhc.noaa.gov/data/tcr/AL252005_Wilma.pdf.

Persing, J., and M. T. Montgomery, 2003: Hurricane superintensity. *J. Atmos. Sci.*, **60**, 2349–2371, https://doi.org/10.1175/1520-0469(2003)060<2349:HS>2.0.CO;2.

Reasor, P. D., R. Rogers, and S. Lorsolo, 2013: Environmental flow impacts on tropical cyclone structure diagnosed from airborne Doppler radar composites. *Mon. Wea. Rev.*, **141**, 2949–2969, https://doi.org/10.1175/MWR-D-12-00334.1.

Rodgers, E. B., W. S. Olson, V. M. Karyampudi, and H. F. Pierce, 1998: Satellite-derived latent heating distribution and environmental influences in Hurricane Opal (1995). *Mon. Wea. Rev.*, **126**, 1229–1247, https://doi.org/10.1175/1520-0493(1998)126<1229:SDLHDA>2.0.CO;2.

Rogers, R. F., 2010: Convective-scale structure and evolution during a high-resolution simulation of tropical cyclone rapid intensification. *J. Atmos. Sci.*, **67**, 44–70, https://doi.org/10.1175/2009JAS3122.1.

——, P. D. Reasor, and J. A. Zhang, 2015: Multiscale structure and evolution of Hurricane Earl (2010) during rapid intensification. *Mon. Wea. Rev.*, **143**, 536–562, https://doi.org/10.1175/MWR-D-14-00175.1.

Rotunno, R., and J. P. Klemp, 1982: The influence of the shear-induced pressure gradient on thunderstorm motion. *Mon. Wea. Rev.*, **110**, 136–151, https://doi.org/10.1175/1520-0493(1982)110<0136:TIOTSI>2.0.CO;2.

——, and K. A. Emanuel, 1987: An air–sea interaction theory for tropical cyclones. Part II: Evolutionary study using a nonhydrostatic axisymmetric numerical model. *J. Atmos. Sci.*, **44**, 542–561, https://doi.org/10.1175/1520-0469(1987)044<0542:AAITFT>2.0.CO;2.

Shapiro, A., S. Rahimi, C. K. Potvin, and L. Orf, 2015: On the use of advection correction in trajectory calculations. *J. Atmos. Sci.*, **72**, 4261–4280, https://doi.org/10.1175/JAS-D-15-0095.1.

Shapiro, L. J., and H. E. Willoughby, 1982: The response of balanced hurricanes to local sources of heat and momentum. *J. Atmos. Sci.*, **39**, 378–394, https://doi.org/10.1175/1520-0469(1982)039<0378:TROBHT>2.0.CO;2.

Skamarock, W. C., and Coauthors, 2008: A description of the Advanced Research WRF version 3. NCAR Tech. Note NCAR/TN-475+STR, 113 pp., https://doi.org/10.5065/D68S4MVH.

Wang, Z., 2014: Characteristics of convective processes and vertical velocity from the tropical wave to tropical cyclone stage in a high-resolution numerical model simulation of Tropical Cyclone Fay (2008). *J. Atmos. Sci.*, **71**, 896–915, https://doi.org/10.1175/JAS-D-13-0256.1.

Wilks, D. S., 2011: *Statistical Methods in the Atmospheric Sciences*. 3rd ed. International Geophysics Series, Vol. 100, Academic Press, 704 pp.

Zhang, D.-L., and R. A. Anthes, 1982: A high-resolution model of the planetary boundary layer: Sensitivity tests and comparisons with SESAME-79 data. *J. Appl. Meteor.*, **21**, 1594–1609, https://doi.org/10.1175/1520-0450(1982)021<1594:AHRMOT>2.0.CO;2.

——, and H. Chen, 2012: Importance of the upper-level warm core in the rapid intensification of a tropical cyclone. *Geophys. Res. Lett.*, **39**, L02806, https://doi.org/10.1029/2011gl050578.

——, Y. Liu, and M. K. Yau, 2000: A multiscale numerical study of Hurricane Andrew (1992). Part III: Dynamically induced vertical motion. *Mon. Wea. Rev.*, **128**, 3772–3788, https://doi.org/10.1175/1520-0493(2001)129<3772:AMNSOH>2.0.CO;2.

——, ——, and ——, 2002: A multiscale numerical study of Hurricane Andrew (1992). Part V: Inner-core thermodynamics. *Mon. Wea. Rev.*, **130**, 2745–2763, https://doi.org/10.1175/1520-0493(2002)130<2745:AMNSOH>2.0.CO;2.

Zipser, E. J., 2003: Some views on ''hot towers'' after 50 years of tropical field programs and two years of TRMM data. *Cloud Systems, Hurricanes, and the Tropical Rainfall Measuring Mission (TRMM)—A Tribute to Dr. Joanne Simpson*, *Meteor. Monogr.*, No. 29, Amer. Meteor. Soc., 49–58.